Characterization of statistical prior image constrained compressed sensing. I. Applications to time-resolved contrast-enhanced CT

Pascal Thériault Lauzier
Medical Physics Department, University of Wisconsin-Madison, Madison, Wisconsin 53705

Guang-Hong Chen[a)]
Medical Physics Department, University of Wisconsin-Madison, Madison, Wisconsin 53705 and Department of Radiology, University of Wisconsin-Madison, Wisconsin, 53705

(Received 13 April 2012; revised 11 July 2012; accepted for publication 8 August 2012; published 12 September 2012)

Purpose: Prior image constrained compressed sensing (PICCS) is an image reconstruction framework that takes advantage of a prior image to improve the image quality of CT reconstructions. An interesting question that remains to be investigated is whether or not the introduction of a statistical model of the photon detection in the PICCS reconstruction framework can improve the performance of the algorithm when dealing with high noise projection datasets. The goal of the research presented in this paper is to characterize the noise properties of images reconstructed using PICCS with and without statistical modeling. This paper investigates these properties in the clinical context of time-resolved contrast-enhanced CT.

Methods: Both numerical phantom studies and an Institutional Review Board approved human subject study were used in this research. The conventional filtered backprojection (FBP), and PICCS with and without the statistical model were applied to each dataset. The prior image used in PICCS was generated by averaging over FBP reconstructions from different time frames of the time-resolved CT exam, thus reducing the noise level. Numerical studies were used to evaluate if the noise characteristics are altered for varying levels of noise, as well as for different object shapes. The dataset acquired *in vivo* was used to verify that the conclusions reached from numerical studies translate adequately to a clinical case. The results were analyzed using a variety of qualitative and quantitative metrics such as the universal image quality index, spatial maps of the noise standard deviations, the noise uniformity, the noise power spectrum, and the model-observer detectability.

Results: The noise characteristics of PICCS were shown to depend on the noise level contained in the data, the level of eccentricity of the object, and whether or not the statistical model was applied. Most differences in the characteristics were observed in the regime of low incident x-ray fluence. No substantial difference was observed between PICCS with and without statistics in the high fluence domain. Objects with a semi-major axis ratio below 0.85 were more accurately reconstructed with lower noise using the statistical implementation. Above that range, for mostly circular objects, the PICCS implementation without the statistical model yielded more accurate images and a lower noise level. At all levels of eccentricity, the noise spatial distribution was more uniform and the model-observer detectability was greater for PICCS with the statistical model. The human subject study was consistent with the results obtained using numerical simulations.

Conclusions: For mildly eccentric objects in the low noise regime, PICCS without the noise model yielded equal or better noise level and image quality than the statistical formulation. However, in a vast majority of cases, images reconstructed using statistical PICCS have a noise power spectrum that facilitated the detection of model lesions. The inclusion of a statistical model in the PICCS framework does not always result in improved noise characteristics. [http://dx.doi.org/10.1118/1.4748323]

Key words: compressed sensing, computed tomography, iterative reconstruction algorithms, maximum a posteriori estimation, dynamic imaging

I. INTRODUCTION

Prior image constrained compressed sensing[1] (PICCS) is an image reconstruction framework that uses an image known *a priori* to regularize the reconstruction procedure. PICCS has been applied to several computed tomography (CT) image reconstruction problems in the last few years.[2–15] Many of these applications involved an undersampled data acquisition. However, in the current work, we investigate the reconstruction of high quality image from fully sampled datasets with a high level of Poisson noise. This is a particularly interesting topic since it could enable a reduction in the ionizing radiation dose imparted to patients during CT exams.

Recently, the PICCS objective function was combined with the well-known penalized-likelihood reconstruction framework.[16] This implementation also incorporated

deformable registration into the reconstruction procedure to enable a more flexible application of PICCS in some clinical settings. One interesting point in that work is the incorporation of a heteroscedastic statistical model—a model that accounts for the different level of variability present in different projections. Generally speaking, iterative reconstruction methods that include a statistical model of photon detection have been shown to improve image noise characteristics in many cases.[17–25] As proposed previously, an explicit noise model can be included into PICCS.[14] However, the impact of photon statistics on the performance of PICCS reconstructions has not been fully evaluated. One factor is worth mentioning here; the use of bow-tie filters in a modern CT scanner flattens the x-ray beam intensity to a large extent across the cross section of the image object. This may mitigate the potential benefits of statistical image reconstruction. In this regard, diagnostic CT differs from emission computed tomography. An extreme example of the impact of the bow-tie filter would be to image a uniform circular object using a perfectly designed filter. One could generate a uniform x-ray beam intensity across the entire detector with no heteroscedasticity. However, when the match is imperfect—such as when the object is not cylindrical or contains region of substantially higher or lower attenuation coefficient— a statistical model could be beneficial.

Two clinically relevant applications are of particular interest in the context of low tube current CT. We are interested in time-resolved dynamic contrast enhanced CT (TR-DCECT), which has been used to enable CT perfusion imaging and time-resolved CT angiography, and in non-time-resolved multi-detector CT (MDCT) which has been widely used in chest and abdominal imaging. Different image characteristics need to be emphasized in these two applications because of the difference between the methods used to generate the PICCS prior image. Therefore, we separate the discussion of these applications in two consecutive papers. The TR-DCECT is discussed in the current paper, while low-dose MDCT will be discussed in a subsequent paper along with an extensive discussion of the spatial resolution properties of the approach.

The development of TR-DCECT has enabled the quantitative assessment of blood perfusion in the brain,[26–29] heart[30,31] and in other organs. In essence, a TR-DCECT exam requires the repetitive scanning of the volume of interest while a contrast agent is administered. The reconstructed images can be analyzed to yield quantitative measures of blood flow (BF), blood volume (BV), and mean transit time (MTT), which may be clinically relevant. While this information is valuable, the radiation dose required to adequately sample the time attenuation curve (TAC) is often high due to repeated scanning. Therefore, there is an urgent need to significantly reduce radiation dose in TR-DCECT.

In recent years, many different methods have been proposed to minimize the exposure to ionizing radiation in TR-DCECT. For example, one may increase the temporal sampling period, thus reducing the number of scans acquired per unit time.[32,33] Several acquisition schemes with view-angle undersampling have also been proposed but they generally require hardware modifications of the scanner.[1,6,34,35] It is also possible to reduce the tube current during the scan, but this approach results in a high level of image noise.

The high noise level of low tube current studies can be reduced by averaging over different time frames. In doing so, however, the temporal dynamics are lost. It is possible to use PICCS with the time-averaged image as prior image to constrain the reconstruction of each individual frame of the time series. PICCS has been shown to enable the reconstruction of images at individual time frames with high temporal resolution from low temporal resolution prior images.[1,6,13,14] The images thus reconstructed display a lower noise level than images produced using the classical filtered backprojection (FBP) algorithm. Although the feasibility of using PICCS to reduce radiation dose in TR-DCECT has been demonstrated in preliminary studies,[1,6,14] several questions need to be investigated to warrant a clinical implementation: How does the inclusion of a statistical noise model influence the noise in images obtained using PICCS? Do noise characteristics change as the photon fluence decreases? Is there a fluence level at which the statistical model improves the performance? Does the shape of the object being imaged influence the results? The goal of this paper is to provide answers to some of these questions.

The paper is structured as follows. Section II reviews the statistical modeling typically used in CT imaging. Section III introduces PICCS and the incorporation of the statistical model in the framework. The quantitative evaluation metrics used in the evaluation are presented in Sec. V. Section IV describes reconstruction algorithms implementation. To enhance readability, the experimental methodology and the results are separated into different sections depending on the datasets used. The numerical studies are presented in Secs. VI, VII and VIII, while the clinical dataset study is given in Sec. IX. Finally, the discussion and conclusions are summarized in Sec. X.

II. STATISTICAL IMAGE RECONSTRUCTION

Statistical image reconstruction aims to obtain an image which matches the projection data in a statistical sense. In order to discuss this framework, let us first define the physical model of the detection system. The distribution of x-ray attenuation coefficients of an image object is defined as a compactly supported function $\mu : \Omega \to \mathbb{R}$, where $\Omega \subset \mathbb{R}^3$ is the spatial support of the object. We define the x-ray projection measurements vector $\mathbf{y} \in \mathbb{R}^{N_{proj}}$, with $[\mathbf{y}]_i = y_i$, storing a set of line integrals over the lines $\{\ell_i \subset \mathbb{R}^3 : i \in [1, N_{proj}]\}$ such that

$$\bar{y}_i = \int_{\ell_i \cap \Omega} ds \mu. \tag{1}$$

For the purposes of numerical representation, the attenuation coefficient distribution is discretized using basis functions $B_j : \mathbb{R}^3 \to \mathbb{R}$ describing the voxelized $M \times N \times P$ image $\mathbf{x} \in \mathbb{R}^{MNP}$ with $[\mathbf{x}]_j = x_j$. We write the voxel approximation as

$$\mu(\mathbf{r}) \approx \sum_{j=1}^{MNP} x_j B_j(\mathbf{x}). \tag{2}$$

In this representation, the approximate x-ray projection—typically called forward projection and denoted by the tilde here—becomes

$$\begin{aligned}\tilde{y}_i &= \int_{\ell_i \cap \Omega} ds \sum_{j=1}^{MNP} x_j B_j(\mathbf{x}) \\ &= \sum_{j=1}^{MNP} x_j \int_{\ell_i \cap \Omega} ds\, B_j(\mathbf{x}) \\ &= \sum_{j=1}^{MNP} A_{ij} x_j,\end{aligned} \tag{3}$$

where $\mathbf{A} \in \mathbb{R}^{N_{proj} \times MNP}$ with $[\mathbf{A}]_{i,j} = A_{ij}$ is the intersection length of line i with voxel j. We thus write $\tilde{\mathbf{y}} = \mathbf{A}\mathbf{x}$.

X-ray detectors do not directly measure $\bar{\mathbf{y}}$ but rather measure the number of photon counts $\mathbf{n} \in \mathbb{N}^{N_{proj}}$ with $[\mathbf{n}]_i = n_i$. Note that we have assumed that a photon counting detector is used for convenience; energy integrating detectors are used in the majority of the modern CT systems. Accounting only for counting statistics, each n_i is statistically distributed according to a Poisson distribution with mean $\bar{n}_i \in \mathbb{R}$ such that

$$\bar{n}_i = f_i \exp(-\bar{y}_i), \tag{4}$$

where, f_i is the x-ray fluence incident on the object. We also define the stochastic projection variables

$$y_i = \log\left(\frac{f_i}{n_i}\right). \tag{5}$$

Generally, in medical CT, the values f_i are not equal to each other due to the bow-tie compensation and to the heel effect of x-ray tubes.[36]

Using the previous notation, the conditional probability for measuring count values $\mathbf{n}$ given an object with attenuation coefficients $\mathbf{x}$ is

$$P(\mathbf{n}|\mathbf{x}) = \prod_{i=1}^{N_{proj}} \frac{\bar{n}_i^{n_i} \exp(\bar{n}_i)}{n_i!}. \tag{6}$$

The log likelihood can be shown[20,24,37] to simplify to

$$L(\mathbf{n}|\mathbf{x}) = -\sum_{i=1}^{N_{proj}} [n_i \tilde{y}_i + f_i \exp(-\tilde{y}_i)]. \tag{7}$$

Using Eq. (5), we can write

$$L(\mathbf{n}|\mathbf{x}) = -\sum_{i=1}^{N_{proj}} [n_i \tilde{y}_i + n_i \exp(y_i - \tilde{y}_i)], \tag{8}$$

which is possible to approximate using a Taylor expansion[20,38] to yield

$$L(\mathbf{n}|\mathbf{x}) = -\frac{1}{2}\sum_{i=1}^{N_{proj}} [(y_i - \tilde{y}_i)^2 n_i] \tag{9}$$

$$= -\frac{1}{2}(\mathbf{y} - \mathbf{A}\mathbf{x})^{\mathrm{T}} \mathbf{D} (\mathbf{y} - \mathbf{A}\mathbf{x}), \tag{10}$$

where $\mathbf{D} \in \mathbb{R}^{N_{proj} \times N_{proj}}$ is a diagonal matrix with the elements of vector $\mathbf{n}$ on its diagonal. The notation $(\bullet)^{\mathrm{T}}$ indicates a matrix transpose.

The vector which maximizes $L(\mathbf{n}|\mathbf{x})$ is called the maximum likelihood (ML) estimate.[18] However, this result is often unstable since it does not incorporate prior information about the image to be reconstructed. It is possible to include this information via a regularizing field $R : \mathbb{R}^{MNP} \to \mathbb{R}$. The vector which solves

$$\hat{x} = \underset{\mathbf{x} \in \mathbb{R}^{MNP}}{\operatorname{argmax}} [L(\mathbf{n}|\mathbf{x}) + R(\mathbf{x})] \tag{11}$$

is called the maximum *a posteriori* (MAP) estimate. The function $R(\mathbf{x})$ will be discussed in Sec. III.

The model proposed by Stayman *et al.*[16] uses the log likelihood given in Eq. (7), while the model used in the research presented here is based on the approximate Eq. (10). An important difference between the two approaches is that the latter requires the computation of the logarithm of the detector data.[39] This function is undefined for $n_i \leq 0$, a case which may occur at ultra low dose if electronic noise is present. A practical means of accounting for this possibility is to use a threshold during the logarithm calculation

$$y_i = \begin{cases} log(f_i/n_i) & \text{for } n_i > \epsilon \\ log(f_i/\epsilon) & \text{for } n_i \leq \epsilon \end{cases}. \tag{12}$$

Here ϵ is a threshold used to regularize the logarithm operation and is often set as the estimated electronic noise level. Furthermore, the approximate log likelihood has been shown to be biased when counts are close to zero. Despite these theoretical shortcomings, the approximate log likelihood has been used successfully in CT applications.[25,38,40] It also has the benefit of being readily implemented in an unconstrained formulation of the PICCS reconstruction framework using a simple nonlinear conjugate gradient algorithm.[14]

III. PRIOR IMAGE CONSTRAINED COMPRESSED SENSING (PICCS) RECONSTRUCTION FRAMEWORK

Compressed sensing (CS) is a signal processing theory which enables the exact recovery of a signal from very few samples, given that the sampling system and the signal possess certain characteristics. Specifically, CS stipulates that if a signal is "sparse" in a known domain and that this domain is "incoherent" with the sampling basis, then the signal can be reconstructed exactly from few samples.[41–43] In practice, the signal is reconstructed by minimizing an objective function that includes a sparsity-promoting norm such as the ℓ_1-norm

$$\hat{\mathbf{x}} = \underset{\mathbf{x}}{\operatorname{argmin}} \|\Psi\mathbf{x}\|_1 \quad \text{s.t. } \mathbf{A}\mathbf{x} = \mathbf{y}, \tag{13}$$

where Ψ is a transformation that sparsifies $\mathbf{x}$, the ℓ_1-norm is defined as $\|\mathbf{x}\|_1 = \sum_i |x_i|$, and $\mathbf{A}$ is the system matrix which describes how the signal $\mathbf{x}$ contributes to the measurements $\mathbf{y}$.

In medical imaging applications, an image similar to that to be reconstructed is often available. This image is referred to as the prior image and its origin depends on the specific clinical application. An appropriate prior image should have

a high signal to noise ratio (SNR) and a low level of artifacts. However, it may differ from the target image—the one aimed by the reconstruction—by containing different structural details, noise level, temporal resolution, spectral resolution, and/or spatial resolution. The goal of PICCS is to integrate this prior image into the CS signal recovery procedure. To this end, the following constrained optimization problem was proposed[1]

$$\hat{\mathbf{x}} = \underset{\mathbf{x}\in\mathbb{R}^{MNP}}{\operatorname{argmin}}[\alpha\|\Psi_1(\mathbf{x}-\mathbf{x}_p)\|_1 + (1-\alpha)\|\Psi_2\mathbf{x}\|_1] \quad \text{s.t. } \mathbf{Ax} = \mathbf{y}, \tag{14}$$

where $\mathbf{x}_p \in \mathbb{R}^{MNP}$ is the prior image, Ψ_1 and Ψ_2 are sparsifying transforms, and $\alpha \in [0, 1]$ is a scalar that controls the relative weight to be allocated to the prior image term and to the original CS term from Eq. (13).

In order to account for the presence of noise in the data, the reconstruction problem was reformulated as an unconstrained optimization procedure[14,16]

$$\hat{\mathbf{x}} = \underset{\mathbf{x}\in\mathbb{R}^{MNP}}{\operatorname{argmin}}[\alpha\|\Psi_1(\mathbf{x}-\mathbf{x}_p)\|_1 + (1-\alpha)\|\Psi_2\mathbf{x}\|_1 - \lambda L(\mathbf{n}|\mathbf{x})], \tag{15}$$

where $\lambda \in \mathbb{R}$ is a scalar which controls the amount of data consistency to be enforced by the algorithm. As previously mentioned, the log likelihood expression used in the research presented in this paper is the approximation given in Eq. (10). Explicitly, the statistical PICCS optimization problem is given as follows:

$$\hat{\mathbf{x}} = \underset{\mathbf{x}\in\mathbb{R}^{MNP}}{\operatorname{argmin}}[\alpha\|\Psi_1(\mathbf{x}-\mathbf{x}_p)\|_1 + (1-\alpha)\|\Psi_2\mathbf{x}\|_1 + \frac{\lambda}{2}(\mathbf{y}-\mathbf{Ax})^{\mathrm{T}}\mathbf{D}(\mathbf{y}-\mathbf{Ax})]. \tag{16}$$

In order to study the effect of the statistical formulation, PICCS was applied using both $\mathbf{D} = \operatorname{diag}\{n_i\}$ and $\mathbf{D} = \mathbf{I}$, where $\mathbf{I}$ is the identity matrix. For the rest of this paper, we refer to the first version as PICCS with statistical weights and to the second as PICCS without statistical weights.

On a philosophical note, it is interesting to note that MAP estimation evolved from ML estimation by the application of Bayes' theorem, which introduced a prior distribution to regularize the optimization problem—$R(\mathbf{x})$ in Eq. (11). This interpretation of the regularization term is in agreement, at least in principle, with CS theory. Indeed, in CS, one attempts to model characteristics of the signal as well as possible in order to obtain a sparse representation. In essence, the goal of ℓ_1 minimization, while not formulated in a fully statistical framework, is the same as the introduction of the prior distribution, i.e., to include *a priori* information about the image into the reconstruction. In PICCS, the assumed prior information is particularly strong, a fact that may also explains its high performance.

IV. RECONSTRUCTION ALGORITHMS IMPLEMENTATION

The implementation of PICCS in this research uses the total variation (TV) (Refs. 38 and 44–50) for both Ψ_1 and Ψ_2 in Eq. (16). The algorithm used to solve the PICCS optimization problem was a simple nonlinear conjugate gradient (NLCG) method.[51] The specifics of the implementation were presented in the literature.[14]

The algorithm was written in C++ and was executed on a workstation equipped with an Intel Core 2 Quad CPU (Intel Corporation, Santa Clara, CA) clocked at 2.66 GHz and 8 GB of RAM. In all cases, 150 NLCG iterations were performed in approximately 400 s for the numerical datasets and in 800 s for the *in vivo* dataset. Note that no parallelization was used in this implementation.

The FBP algorithm used a Shepp-Logan filter and a fan-beam geometry.

V. EVALUATION METRICS

As we emphasized before, the primary aim of this research is to characterize the noise properties presented in images reconstructed using PICCS with and without the statistical weights matrix $\mathbf{D}$. The approach we took in this study can be considered empirical, i.e., we implemented an optimization algorithm to find the minimizer of the PICCS objective function for a number of different datasets. Numerically simulated projection datasets are utilized because of their flexibility and the existence of a ground truth for comparison. An *in vivo* dataset is also used to verify that the conclusions reached in the numerical studies are consistent with a clinical case.

Many metrics have been developed to describe image quality and characterize the noise present in images, although there is no consensus yet on what are the most appropriate metrics to assess iteratively reconstructed images. We chose a number of these metrics based on their applicability to tomographic images.

V.A. Noise level and uniformity

In order to evaluate the noise level and uniformity, the noise standard deviation was measured as follows:

$$\sigma = \sqrt{\langle (x - \langle x\rangle)^2\rangle}, \tag{17}$$

where the operation $\langle\bullet\rangle$ represents the ensemble average. For the numerical studies, the noise standard deviation was measured independently for each image pixel by averaging over $N_n \in \mathbb{N}$ distinct reconstructions each with a distinct noise realization

$$\sigma_{r_1,r_2} \approx \sqrt{\frac{1}{N_n - 1}\sum_{i=1}^{N_n}(x_{r_1,r_2} - \mu_{r_1,r_2})^2}, \tag{18}$$

where

$$\mu_{r_1,r_2} = \frac{1}{N_n}\sum_{i=1}^{N_n} x_{r_1,r_2}^{(i)}. \tag{19}$$

$\mathbf{x}^{(i)}$ denotes the image with the ith noise realization.

For *in vivo* studies, the above ensemble average cannot be performed. Therefore, the noise standard deviation is measured over pixels within a region of interest (ROI) containing only noise. In that case,

$$\sigma_{ROI} \approx \sqrt{\frac{1}{N_{ROI}-1}\sum_{(r_1,r_2)\in ROI}(x_{r_1,r_2}-\mu_{ROI})^2}, \tag{20}$$

where

$$\mu_{ROI} = \frac{1}{N_{ROI}}\sum_{(r_1,r_2)\in ROI} x_{r_1,r_2}, \tag{21}$$

and N_{ROI} is the number of pixels contained within the ROI.

The noise uniformity is an important factor which may differ between images reconstructed using different algorithms. In order to quantify this effect, the noise standard deviation was measured over N_r ROIs scattered across the image. The coefficient of variation c_σ of the standard deviation is then used as a metric of noise uniformity

$$c_\sigma = \frac{1}{\mu_\sigma}\sqrt{\frac{1}{N_r-1}\sum_{i=1}^{N_r}(\sigma_i-\mu_\sigma)^2} \tag{22}$$

where μ_σ is the mean noise standard deviation over all ROIs. A low value of c_σ corresponds to a uniform noise level.

V.A.1. Noise power spectrum (NPS)

The noise power spectrum, also called Weiner spectrum, describes the frequency distribution of the noise power. We define the NPS, P_{k_1,k_2}, as

$$P_{k_1,k_2} = \langle |\mathrm{DFT}_2\{\mathbf{x}\}_{k_1,k_2}|^2\rangle, \tag{23}$$

where $\mathbf{x}$ is the image extracted from an ROI, $k_1 \in [0, N_1 - 1]$ and $k_2 \in [0, N_2 - 1]$ are spatial frequency discrete indices and $r_1 \in [0, N_1 - 1]$ and $r_2 \in [0, N_2 - 1]$ are spatial position discrete indices. We define the 2D discrete Fourier transform (DFT_2) and inverse Fourier transform (IDFT_2) pair as follows:

$$\begin{aligned}\hat{x}_{k_1,k_2} &= \mathrm{DFT}_2\{\mathbf{x}\}_{k_1,k_2}\\ &= d_{r_1}d_{r_2}\sum_{r_1=0}^{N_1-1}\sum_{r_2=0}^{N_2-1} e^{-i2\pi(k_1r_1+k_2r_2)}x_{r_1,r_2}\\ x_{r_1,r_2} &= \mathrm{IDFT}_2\{\hat{\mathbf{x}}\}_{r_1,r_2}\\ &= d_{k_1}d_{k_2}\sum_{k_1=0}^{N_1-1}\sum_{k_2=0}^{N_2-1} e^{i2\pi(k_1r_1+k_2r_2)}\hat{x}_{k_1,k_2},\end{aligned}$$

where the discrete grid spacings d_{r_1}, d_{r_2}, d_{k_1}, and d_{k_2} follow $d_{r_1}d_{k_1} = 1/N_1$ and $d_{r_2}d_{k_2} = 1/N_2$. The operation $\langle\bullet\rangle$ represents the ensemble average. For the purpose of this paper, we approximate the ensemble average by the sample average, i.e., by averaging over a finite number of distinct noise realizations. In the numerical studies presented in this paper, a finite number N_n of noise realizations were simulated in order to approximate the ensemble average as follows:

$$P_{k_1,k_2} \approx \frac{1}{N_n}\sum_{i=1}^{N_n}\left|\mathrm{DFT}_2\{\mathbf{x}^{(i)}\}_{k_1,k_2}\right|^2, \tag{24}$$

where $\mathbf{x}^{(i)}$ denotes the ith noise realization.

In the *in vivo* studies, the NPS was approximated by averaging over power spectra computed from a finite number of uniform regions $N_r \in \mathbb{N}$ of equal dimensions at different locations in the image

$$P_{k_1,k_2} \approx \frac{1}{N_r}\sum_{j=1}^{N_r}\left|\mathrm{DFT}_2\{{}^{(j)}\mathbf{x}\}_{k_1,k_2}\right|^2, \tag{25}$$

where ${}^{(j)}\mathbf{x}$ denotes the j^{th} distinct region.

Note that in the numerical simulations, the noise process is assumed to be stationary within the region under investigation. In the case of the *in vivo* studies, it is assumed that the noise process is stationary over all regions included in the average. Neither of these assumptions are strictly correct, but they provide an approximation that still enables the characterization of the noise.

For linear algorithms such as FBP, one can derive an analytical expression for the NPS of the image produced. However, when it comes to non-linear iterative algorithms such as PICCS, the derivation of an analytical expression for the NPS remains an open question. The approach taken in this research is empirical in the sense that the NPS is calculated from reconstructed images without theoretical analysis.

V.B. Model observer detection task

The detectability of objects depends not only on the contrast to noise ratio (CNR), but also on the specific spatial structure of the noise and signal present in the image. In order to quantify the effect of noise structure, it is possible to compute a detectability index based on the NPS. For simplicity, a non pre-whitening (NPW) observer model is used to evaluate the detectability index d' of a model lesion $\mathbf{s} \in \mathbb{R}^{N_1,N_2}$. We define the detectability index as:[52]

$$d' = \frac{\sum_{k_1}\sum_{k_2}|\hat{s}_{k_1,k_2}|^2}{\sqrt{\sum_{k_1}\sum_{k_2}P_{k_1,k_2}|\hat{s}_{k_1,k_2}|^2}}, \tag{26}$$

where $\hat{\mathbf{s}} = DFT\{\mathbf{s}\}$. When dealing with correlated noise, the NPW observer model has been shown to approximate human observers more accurately than pre-whitening models.[53–59] CT images have correlated noise due to the reconstruction procedure[60,61] and thus, a NPW observer model is expected to be more consistent with a human observer.[62] Furthermore, the noise of CT images is often non-stationary,[61] i.e., it varies spatially. In the numerical studies presented in this paper, we assume that the noise is stationary within the ROI being studied. However, in the *in vivo* studies, the NPS is estimated by averaging over several regions of the image and thus d' may not be fully representative of the local detectability and thus the results should be interpreted accordingly.

The goal of this evaluation is to isolate the effect of the local NPS on the detectability of objects. The impact of the spatial resolution characteristics is not evaluated. This

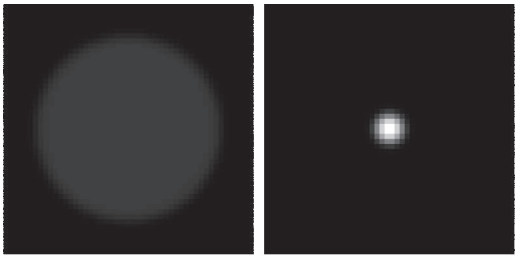

(a) Large test object (b) Small test object

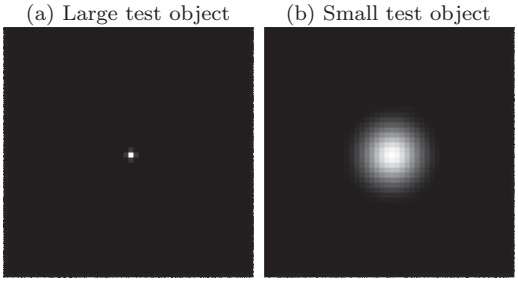

(c) Power spectrum of large test object (d) Power spectrum of small test object

FIG. 1. Model lesion signals used to measure the detectability d' with their associated power spectra.

explains why the detectability model that was chosen for this evaluation does not include the modulation transfer function (MTF). Two model lesions were investigated: a small, high-contrast disk and a large, low-contrast disk. The model lesions were assumed to be signal known exactly (SKE), and therefore were not reconstructed using the algorithm. This was a deliberate choice to avoid complications linked with the shift-variant nature of the MTF for nonlinear reconstruction algorithms. In each case, the signals **s** were generated over a finely sampled grid and were smoothed using a Gaussian blur for anti-aliasing purposes. The signals were then downsampled using cubic spline interpolation in order to match the dimension of the region from which the NPS was measured. Figure 1 shows the two signals and their power spectra.

Due to the above limitations, the value of the detectability metric was not meant to be absolute. Rather, it is a relative metric of detectability that allows one to compare the effect of the NPS in different contexts.

V.C. Image quality

Several characteristics of an image can be said to contribute to its quality. Distortions come in many different forms. The universal image quality index[63] (UQI) was proposed to quantify degradation in the linear correlation, mean luminance, and contrast level relative to a reference image. The UQI is defined in the range [–1, 1]; 1 signifies perfect positive correlation with the reference image, 0 means an absence of correlation between the images, and –1 signifies perfect negative correlation. Mathematically, it is defined as

$$UQI = \frac{4\sigma_{ab}\mu_a\mu_b}{(\sigma_a^2+\sigma_b^2)(\mu_a^2+\mu_b^2)}, \tag{27}$$

where

$$\sigma_{ab} = \frac{1}{N_{ROI}-1}\sum_{i\in ROI}(a_i-\mu_a)(b_i-\mu_b),$$

μ_a and μ_b are the mean image values within the ROI, and σ_a and σ_b are the standard deviations within the ROI.

The UQI was measured for both the numerical and the *in vivo* studies. In the prior, it is measured within an ROI that contains the contrast-enhancing details of the phantom taking a noiseless FBP reconstruction as a reference. In the *in vivo* case, the UQI is measured in a uniform ROI in the corpus callosum taking the temporally averaged prior image as a reference.

The UQI was used in the choice of the data consistency parameter λ from the PICCS objective function. The value of λ that offered the highest UQI was used for the evaluation. This method is motivated in Sec. VI below.

V.D. Spatial resolution

In order to motivate the use of the UQI to select the optimal data consistency parameter λ, we performed a simple noise versus spatial resolution trade off evaluation. We fitted the intensity profile along several edges with the point spread function corresponding to a Gaussian blur. We extracted the width of the corresponding blurring function, which we refer to as the pseudo point-spread function (PSF) width.[13,14] This metric can be measured locally in the image and can thus be used to evaluate the blurring of structures of different size and contrast.

Specifically, for an image under study **x** of dimension $M \times N$, the blur was quantified as follows:

(1) Select a 1D linear segment ℓ through the object of interest in the image.
(2) Solve the least squares problem

$$\min_{b\in\mathbb{R},h\in\mathbb{R}}\sum_{i\in\ell}\left(x_i - hG_b^\ell[\mathbf{x}^{ref}]_i\right)^2,$$

where i is the position in the image matrix, and h is a multiplicative factor. The blurred image, $\mathbf{G}_b^\ell[\mathbf{x}^{ref}] \in \mathbb{R}^{MN\times 1}$, is the convolution of the reference image with a normalized Gaussian function of width b. The image at 2D position (m,n) is

$$G_b^\ell[\mathbf{x}]_{m+nM} = \sum_j\sum_k\left\{x_{k+jM}\frac{1}{2\pi b^2}\times\exp\left[\frac{[(k-m)\Delta_1]^2}{2b^2}\right]\times\exp\left[\frac{[(j-n)\Delta_2]^2}{2b^2}\right]\right\},$$

where Δ_1 and Δ_2 are the voxel dimension along the image horizontal and vertical axes. The value of b that solve the least squares problem above is used as metric of image sharpness. It is referred to as pseudo PSF width for the rest of this paper.

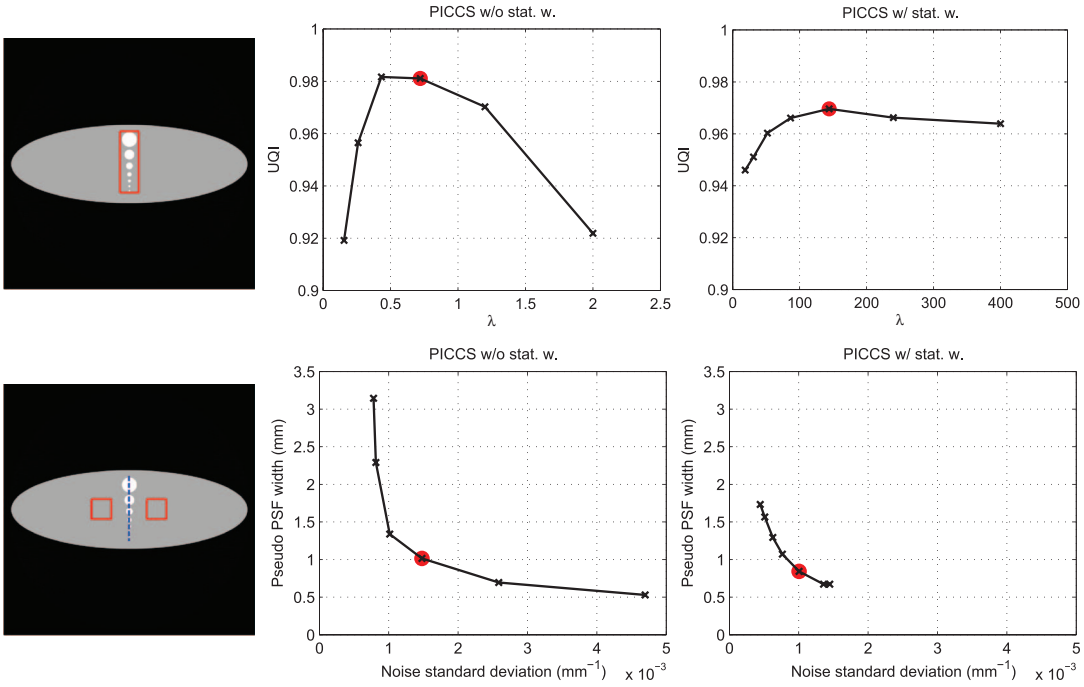

FIG. 2. Illustration of the noise versus spatial resolution tradeoff for various values of data consistency parameter λ. The UQI quantified both noise and spatial resolution. The λ value that provided the optimal UQI is denoted by a bold circle. The UQI was measured in the ROI shown in the upper left image. The pseudo PSF width was measured along the dotted line segment shown in the lower left image. In that same image, the ROIs used to measure the noise standard deviation are also shown.

As mentioned in other publications,[13,14] the pseudo PSF width is modeled using a symmetric Gaussian kernel, which could slightly over- or under-estimate the true local impulse response has a different profile. The results should be evaluated in this context.

Let us emphasize again that the pseudo PSF width was only used to motivate the use of the UQI for λ selection. The issue of spatial resolution will be evaluated more extensively in the second paper of this series.

VI. NUMERICAL STUDY: CHOICE OF DATA CONSISTENCY PARAMETER

VI.A. Methods and materials

The choice of the data consistency parameter λ was done by using the value that yielded the highest UQI. The UQI quantifies the noise, spatial resolution, and texture correlation between two images. In order to motivate this method and characterize the image with the optimal UQI, a numerical phantom study was performed. The pseudo PSF, noise standard deviation, and UQI were measured for a set of images reconstructed at different values of λ.

The eccentricity phantom—used also in the evaluation of the dependence on the object eccentricity—with a semi-major axes ratio of 1/3 was used for this demonstration. The methodological details of the numerical study are presented in more details in Secs. VII and VIII.

Note that this method of selecting λ can only be applied *a posteriori*, i.e., after a series of image has been reconstructed. *A priori* selection—before the reconstruction is performed—is not addressed here.

VI.B. Results

Figure 2 illustrates that the value of the data consistency parameter λ that yielded the highest UQI was also favorable in terms of the trade off between noise and spatial resolution. We note however that the UQI is likely affected by other factors than noise and sharpness. This is apparent in the slightly higher UQI obtained using PICCS without statistical weighting even though the noise and spatial resolution characteristics of this image are not as favorable as those obtained for reconstruction that included statistical weights. An exhaustive evaluation of this behavior is out of the scope of this paper. However, these results presented here support the use of the optimal UQI for the choice of λ for the rest of this paper.

VII. NUMERICAL STUDY: DEPENDENCE ON NOISE LEVEL

VII.A. Methods and materials

Numerical datasets were generated to simulate different clinical situations. The contrast levels of the prior and target images were selected to simulate a TR-DCECT scan with iodinated contrast agent injection. In all cases, the prior image was generated with a lower noise level and objects with a different contrast from those of the target image. Both of these characteristics simulated a temporal averaging procedure that includes images recorded before and after the arrival of

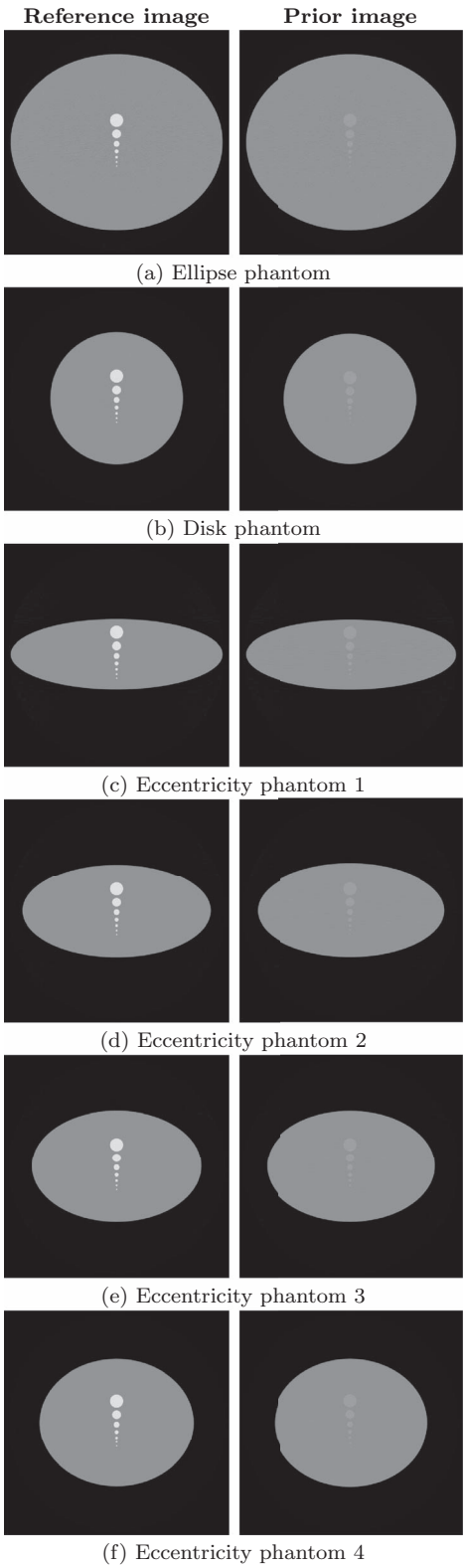

FIG. 3. Reference and prior images for all numerical studies.

contrast agent. The higher contrast of the target image simulated a specific time point at peak arterial contrast concentration. Figure 3 shows all numerical phantoms simulated.

There is no spatial blur being simulated in the prior image. This corresponds to the case of an ideal TR-DCECT exam without any misregistration from one time frame to another during the entire data acquisition. In practice, if motion occurs in the object during the acquisition, a registration procedure may be needed to correct the misalignment before the prior image is generated.

In order to study the effect of the level of noise present in the data, two numerical phantoms were simulated. The first was made of an ellipse, while the second was a circular disk. Each phantom contained circular objects of various sizes. These objects had a coefficient of attenuation that varied between the prior and the target images to simulate a dynamic contrast enhancement.

For all numerical simulations, the scanning geometry was left unchanged. Total 886 projections were simulated for each of 512 view angles. The image matrix size was 512×512 with a pixel size of $(1\ \text{mm})^2$. Furthermore, to enable the computation of noise power spectra, all phantom were also simulated without the dynamic objects. The same reconstruction parameters used for the dynamic reconstructions were used to reconstruct the background datasets. The small dynamic objects were assumed to have a negligible contribution to the statistics of the detection procedure.

VII.B. Results

The reconstruction of the numerical phantoms that were simulated with various levels of noise are shown in Fig. 4. Only the two highest noise levels are shown. The data consistency parameter was set to the value which yielded the most accurate estimate of the dynamic structures in terms of UQI.

The sharpness of the dynamic structures differs between the different reconstruction algorithms and noise levels. This is an important point since these had a different attenuation coefficient between the prior and the target images. As expected, for an increased photon counts, the visualization of these structures improves. Furthermore, the appearance of the objects differs depending whether the statistical weights were applied or not. Indeed, the PICCS reconstruction without the statistical weights showed a slight amount of noise streaks that interfered with the appreciation of the objects. The reconstructions with the statistical weights were not affected by streaks but showed a certain amount of blur around dynamic structures. These observations are reflected by the UQI measurements shown in Fig. 5. The UQI shows an improvement in image quality as the incident photon fluence increases as expected. While this improvement is drastic for FBP, it is much less significant for PICCS. Also, note that for the elliptical phantom, the UQI varies only very slightly between the two versions of PICCS implementation investigated. However, for the circular phantom, PICCS without the statistical weights outperforms the version which includes them. This may not have been expected. The dependence on the shape of the object will be further discussed in Sec. VIII.

Let us now discuss the difference in noise level between the different algorithms. The CNR at several incident fluence levels is shown in Fig. 6. In all cases PICCS outperforms FBP, as was expected. However, it might have been expected that the implementation with statistical weights would have performed better than that without. This is not always the case.

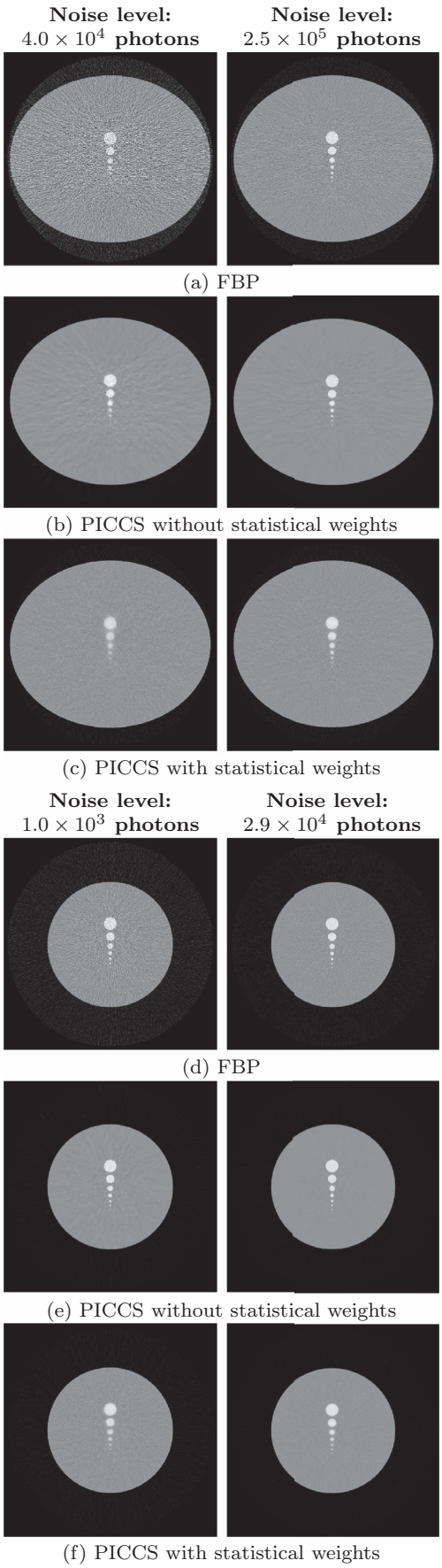

FIG. 4. Reconstructions of the numerical studies with two levels of noise. The reconstructions have a display range of [0.00, 0.04] mm^{-1}.

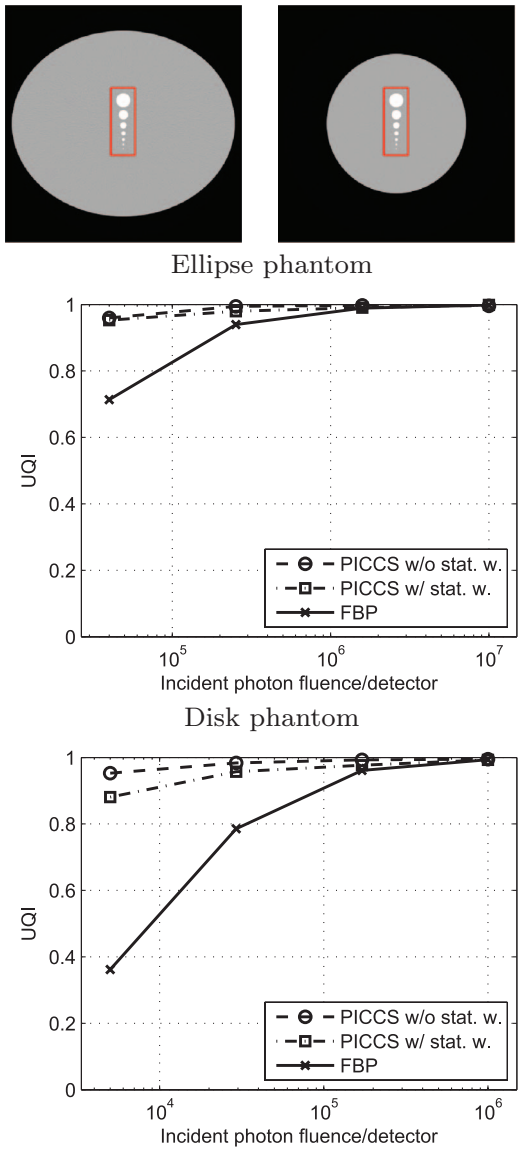

FIG. 5. UQI measured for the elliptic and the disk phantoms. The ROI used for the measurements are shown.

The implementation without statistical weights yielded images with a lower noise level for the disk phantom. This phantom has a relatively low level of heteroscedasticity in the data, i.e. the noise level does not vary dramatically between different projections. Note that the cases shown here constitute a crossover point in terms of object shape; for objects with more eccentricity, PICCS with the statistical weights yields lower noise levels. This will be shown in Sec. VIII.

Another characteristic that differs between the two implementations of PICCS is the spatial noise uniformity. To demonstrate this behavior, noise standard deviation maps were computed using a Monte Carlo approach, over 50 different noise realizations. The maps are shown for Both PICCS implementations in Fig. 7. The gray scale intensity displayed is proportional to the local noise standard deviation. One can observe that each method yields noise distributions with different properties. When the weights were not employed, a high level of non-uniformity is observed, while when they

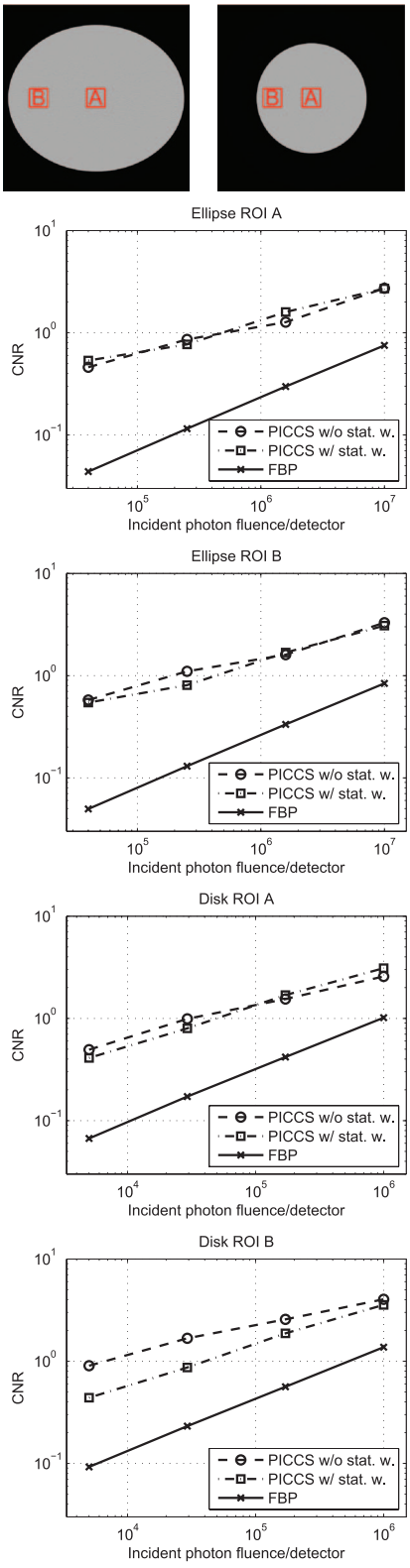

FIG. 6. Contrast to noise ratio (CNR) for the elliptical and circular numerical phantoms. The CNR was measured for the large low-contrast test signal.

were, the noise level is mostly constant across the phantom. Around the edges of the phantom, the noise level drops substantially when the statistical weights are not used. Also, the noise is relatively higher along the axis of the ellipsoidal phantom.

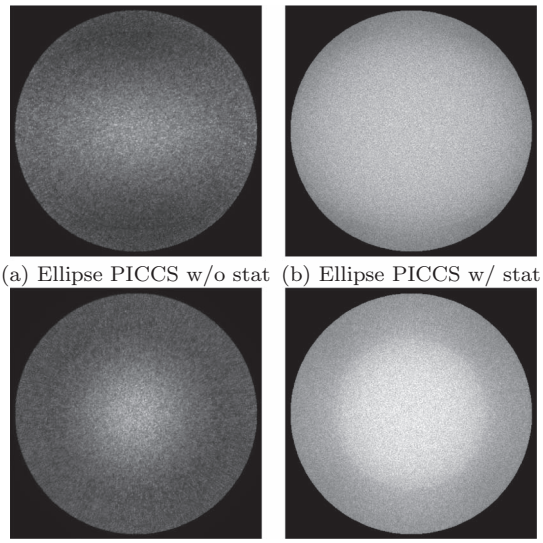

FIG. 7. Maps of the standard deviation for the elliptical and circular numerical phantoms. The display range is the same for each phantom presented.

The non-uniformity was quantified by the noise uniformity metric shown in Fig. 8. A high value of c_σ corresponds to a high level of non-uniformity. The ROIs used for this measurement were each 16 × 16 pixels across. Notably, the implementation of PICCS without statistical weighting resulted in images with more noise non-uniformity than those reconstructed using FBP. Furthermore, the noise uniformity showed only a weak dependence on the incident photon fluence. Such a noise uniformization was observed in other statistical image reconstruction frameworks.[64,65] Thus, it is unlikely that this behavior is specific to PICCS.

Noise level is only one characteristic that influences the ability of an observer to detect objects in noisy images. The spatial frequency composition of the noise background can also have an effect on the detectability of objects. As one can observe from the images of Fig. 4, the structure of the background is different for FBP and both versions of PICCS. To analyze this property, the NPS of the noise background was calculated for the reconstructions obtained from each algorithm. In order to obtain a local representation of the spatial frequency content, the NPS was measured locally within three different ROIs by averaging over 50 different noise realizations. The NPS measurements are shown in Fig. 9. For all NPS figures presented, the zero frequency is located at the center of the image.

As was demonstrated by Baek and Pelc,[61] the noise is nonstationary for images reconstructed from fan-beam projection data using an FBP reconstruction algorithm. Consequently, the NPS varies for different positions within the image. Our results exhibit the same behavior. In particular, one can observe a preferential distribution of the noise in spatial frequencies perpendicular to high noise projections. In image space, this translates in "noise streaks" parallel to high noise projections. Furthermore, since the orientations of high noise projections varies between different locations in the image, this results in an NPS which is location dependent. Interestingly,

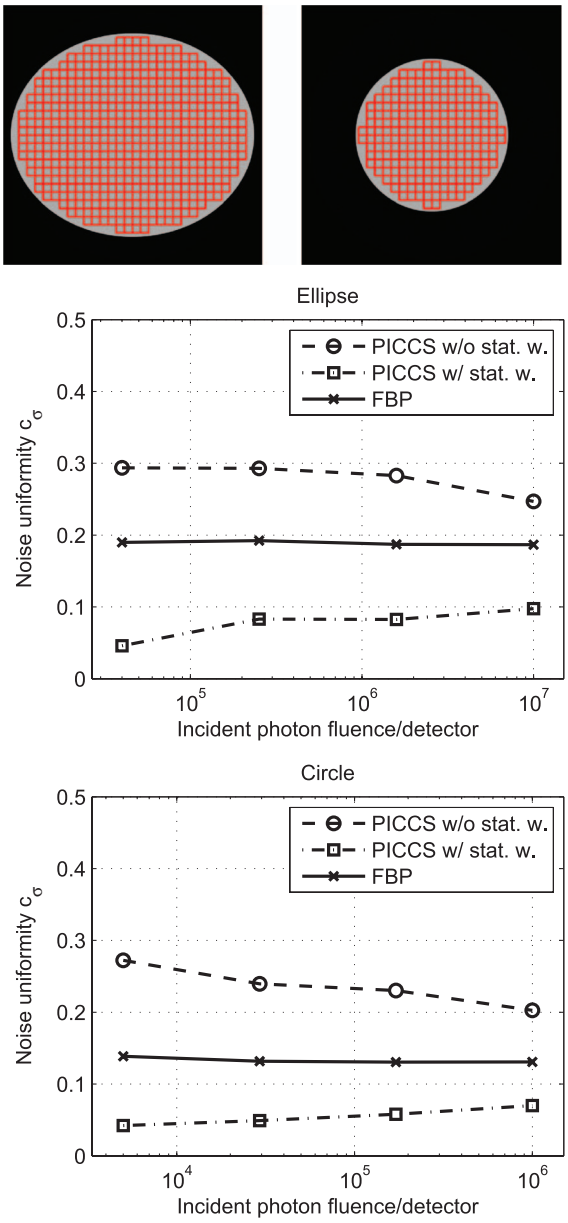

FIG. 8. Noise uniformity metric for the elliptical and circular numerical phantoms as various noise levels. The ROIs used for the measurements are shown.

this anisotropy is also seen in images reconstructed using PICCS, although to a lesser extent than for FBP.

NPS obtained from PICCS with and without statistical weights show some differences. In particular, when no statistical weighting is applied, the noise is more concentrated in low frequencies; the spectrum extends to higher frequencies for the statistical version. This behavior is also visible in image space. Indeed, one can observe on Fig. 4 the structured noise in the PICCS reconstructions without statistical weighting.

An interesting question is to what extent the noise structure affects the detectability of objects. This question was investigated using model observer based detectability. The NPW detectability d' was measured for several ROIs for each lesion models. The results are shown in Figs. 10 and 11. Several characteristics of these curves are worthy of emphasis. First, in all cases, PICCS outperformed FBP. Since the method for computing d' did not use a normalized NPS, this difference is mostly attributable to a difference in noise level. Second, the two versions of PICCS differ mainly in the low count range and the difference disappears at higher counts. In all cases except for the region at the edge of the disk phantom (ROI B on Fig. 11), PICCS with the statistical weight resulted in a higher detectability. Generally, this suggests that the noise structure of images reconstructed with statistical weighting interferes less with the detection of objects. However, the difference fades as the incident fluence increases.

To summarize the results of this section, the PICCS implementation with statistical weighting yielded higher noise levels at the periphery of the phantom, but a more uniform noise spatial distribution with a NPS that aided in the detection of objects. However, the difference between both versions of PICCS studied is mostly observed in the low photon fluence regime.

VIII. NUMERICAL STUDY: DEPENDENCE ON OBJECT ECCENTRICITY

VIII.A. Methods and materials

The effect of the object's shape was studied using a second elliptical phantom. The lengths of the ellipse's semi-major axes were varied while keeping their sum equal. This had the effect of varying the level of noise present in different view angles. The parameters used to construct the numerical phantoms are given in Table I. The rest of the methodological details are shared with the numerical study with respect to the level of noise presented above in Sec. VII.A.

VIII.B. Results

The simulated datasets with varying levels of object eccentricity were reconstructed using both algorithms. The images are presented in Fig. 12. Also presented in this figure are maps of the standard deviation. First, we note that the sharpness of the dynamic objects varied depending on the level of eccentricity and on the algorithm used. For PICCS without statistical weighting, the objects show noise streaks, which are mitigated as the semi-major axis ratio approaches 1. In the case of PICCS with statistical weighting, the reconstructions do not contain noise streaks. Such a streak-mitigation property was also observed by other groups.[66] However, as it was observed for the study of noise level, the images show some blur near the dynamic structures. These observations were quantified to some extent by the UQI, the measurements of which are presented in Fig. 13. PICCS without statistical weighting yielded a slightly higher UQI for more circular phantoms. This result is consistent with the observations from Fig. 5.

The level of object eccentricity also influenced the level of noise present in images. The CNR measured for each implementation of the PICCS algorithm for different values of the semi-major axis ratio is shown in Fig. 14. The measurement of the noise standard deviation was performed by averaging

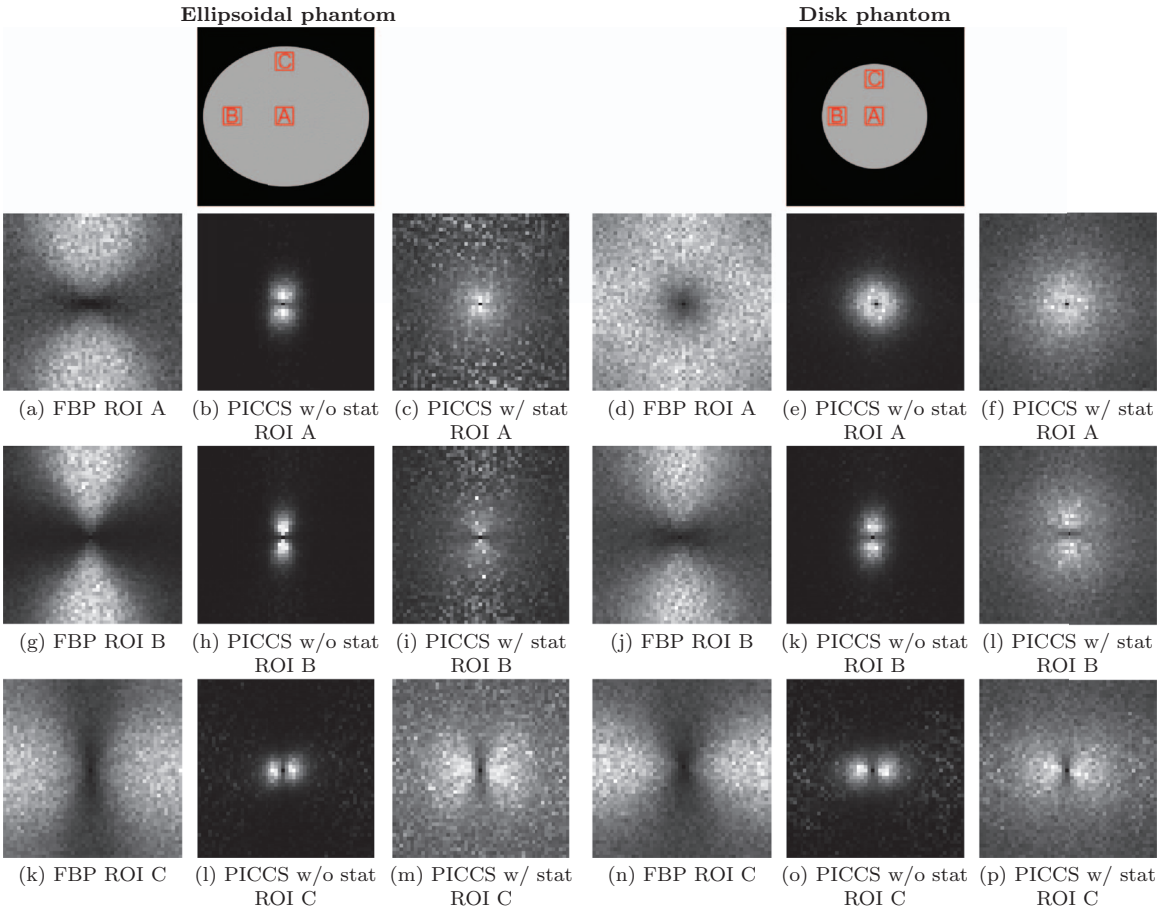

FIG. 9. Noise power spectra for the elliptical and circular numerical phantoms. The display range was set from the minimum to maximum value of each image. The ROIs used for the measurements are shown.

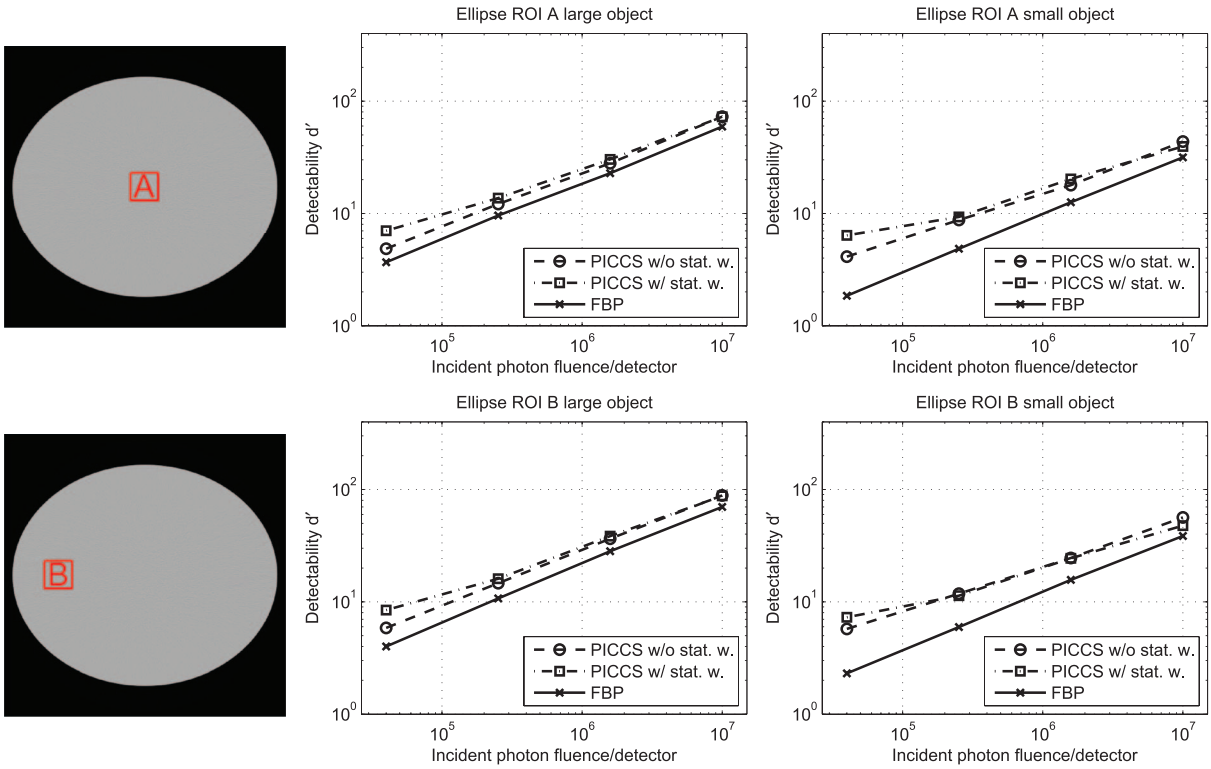

FIG. 10. Detectability for elliptic numerical phantom. The ROIs used for the measurements are shown.

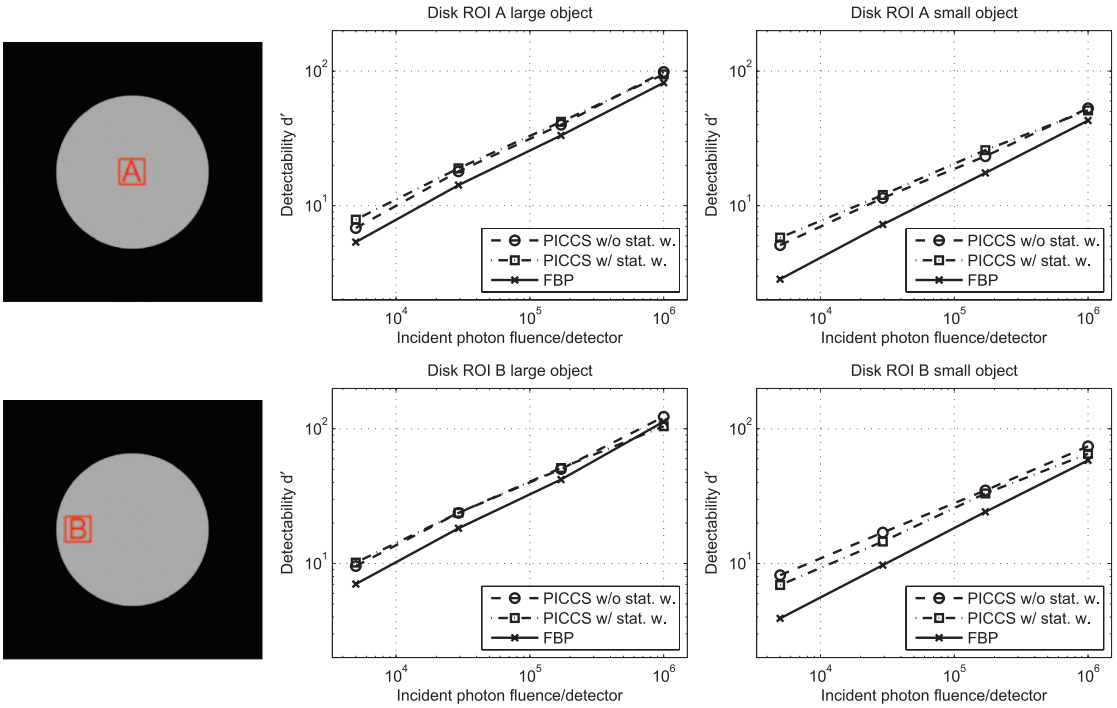

FIG. 11. Detectability for disk numerical phantom. The ROIs used for the measurements are shown.

the noise level from the standard deviation maps in a 50 × 50 voxel ROI at the center of the phantoms. Note that the noise level of FBP and PICCS images with statistical weighting was mostly stable for different eccentricity levels. However, the noise level of PICCS without statistical weighting improved for more circular objects

As shown in Fig. 15, the noise spatial distribution displayed a different behavior for each algorithm. Images reconstructed using PICCS with statistical weighting showed the most uniform noise distribution, which was to a large extent constant for objects with different eccentricity. When the weighting was not applied, the noise varied considerably more between different regions of the image with a general trend towards more uniformity for more circular objects. Qualitatively, these observations are consistent with the appearance of noise standard deviation maps from Fig. 12.

Another observation from Fig. 12 is that the structure of the noise varies depending on the amount of eccentricity. In

TABLE I. Phantom parameters.

	Semi-major axes (mm)		Attenuation coefficient (mm^{-1})			Incident fluence (photons/detector)	
				Details	Details		
Phantom	Horizontal	Vertical	Background	Prior image	Target image	Prior image	Target image
Ellipse	240	200	0.020	0.022	0.035	1.0×10^7	4.0×10^4 2.5×10^5 1.6×10^6 1.0×10^7
Disk	150	150	0.020	0.022	0.035	1.0×10^6	1.0×10^3 2.9×10^4 1.7×10^5 1.0×10^6
Eccentricity	240 213 192 175	80 107 128 145	0.020	0.022	0.035	5.0×10^6	2.0×10^4

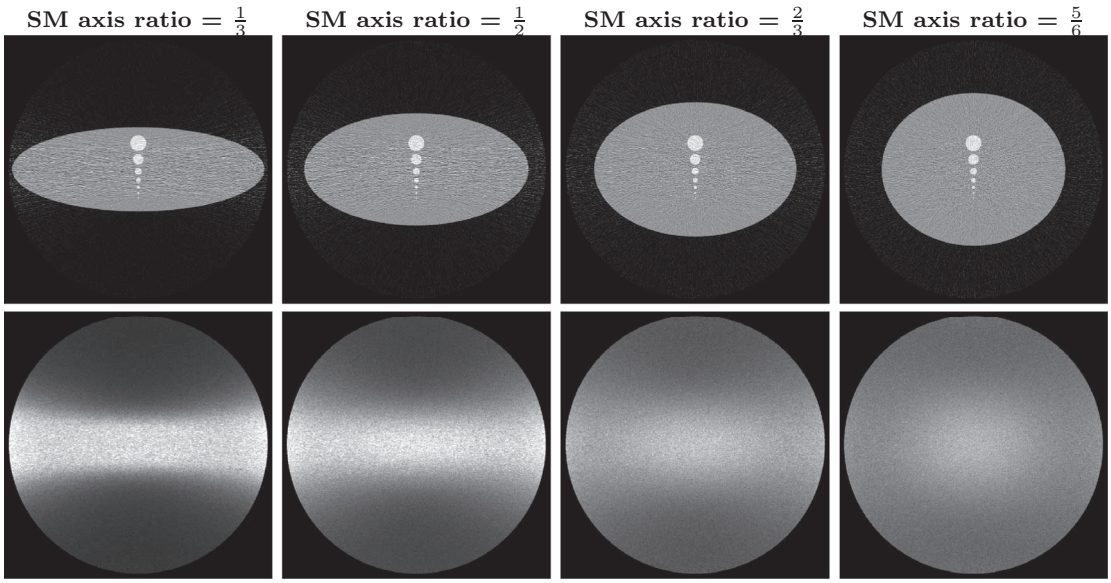

(a) FBP reconstructions

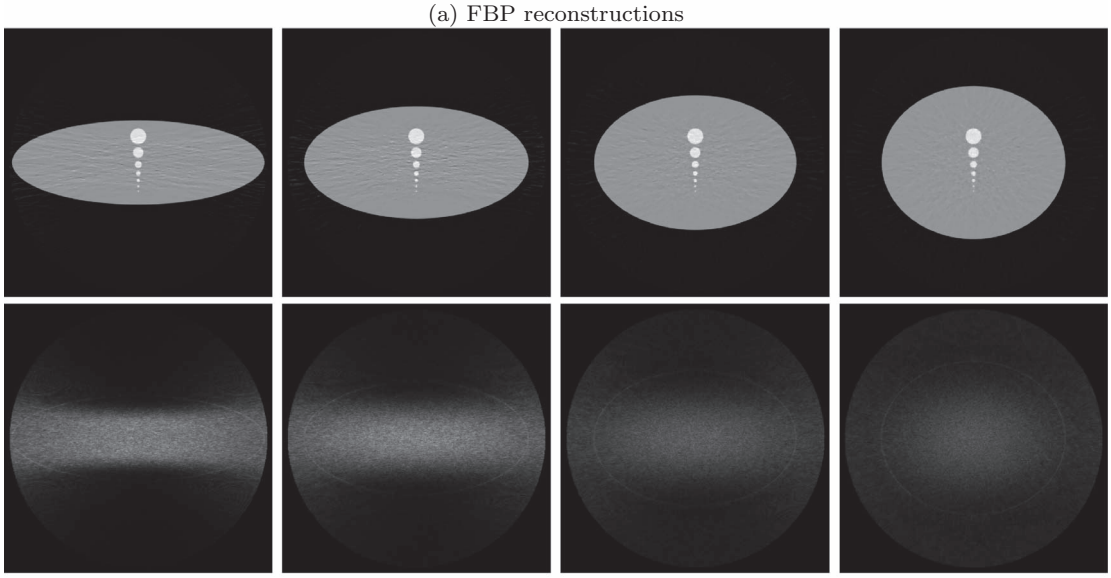

(b) PICCS reconstructions without statistical weights

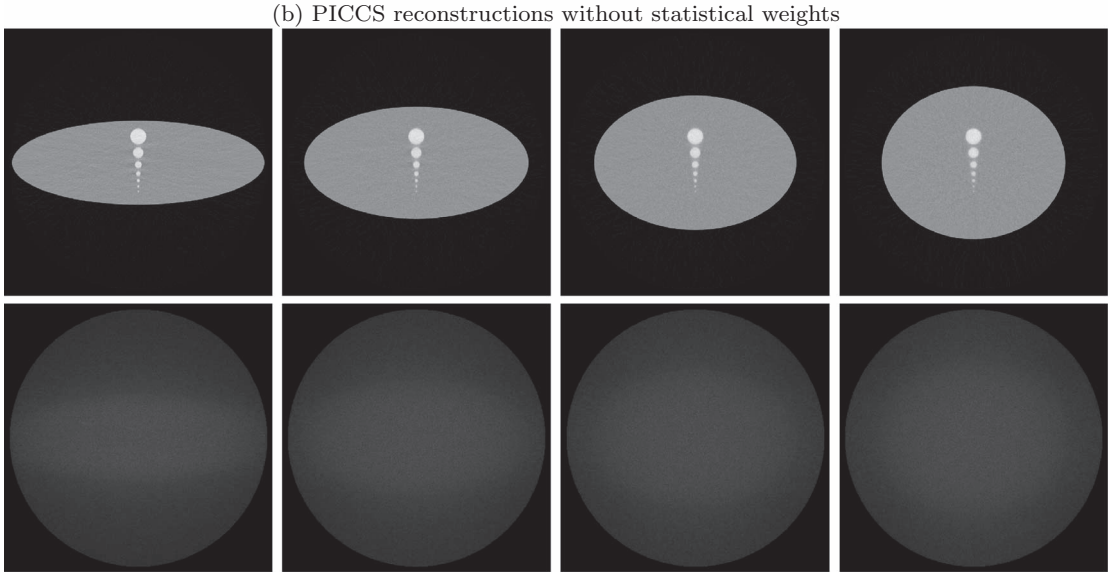

(c) PICCS reconstructions with statistical weights

FIG. 12. Reconstructions with various levels of eccentricity. Each reconstruction is presented with the associated standard deviation map. The reconstructions have a display range of [0.00, 0.04] mm^{-1}, while that of the standard deviation maps is [0.000 0.007] mm^{-1}.

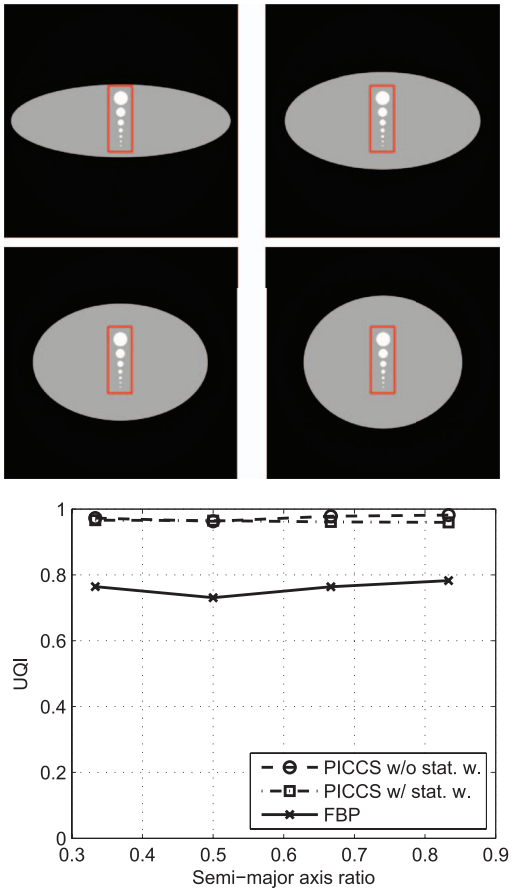

FIG. 13. UQI measured for the eccentricity phantom.

particular, for highly eccentric objects the noise presents itself as streaks parallel to high noise projections—horizontally in this case. This behavior can be clearly appreciated from the NPS computed from these datasets as shown in Fig. 16. These NPS were measured in a 50 × 50 voxel ROI as the center of the phantom using 50 different noise realizations. For highly eccentric objects the noise is concentrated in frequencies perpendicular to high noise projections, an appearance that is mitigated when the object is more circular. This anisotropy is notably mitigated for images reconstructed using PICCS with statistical weighting.

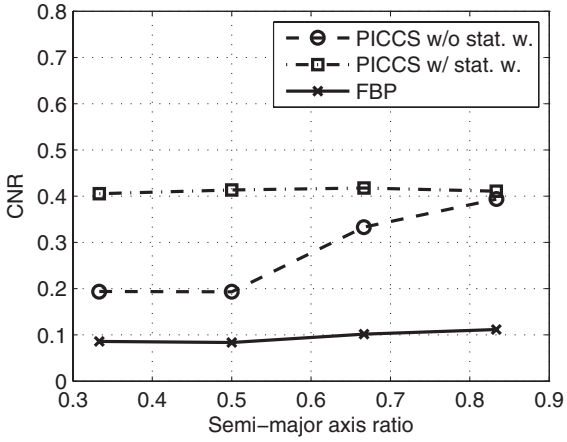

FIG. 14. Contrast to noise ratio at various eccentricity levels.

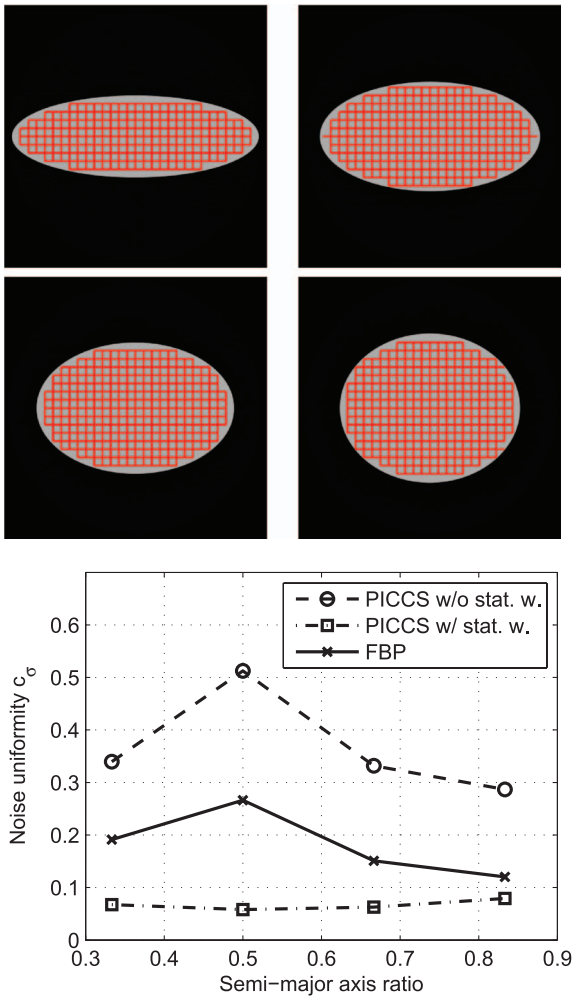

FIG. 15. Noise uniformity metric at various eccentricity levels. The ROIs used for the measurements are shown.

In order to quantify the impact of the noise structure observed from the NPS of each image on the ability of an observer to detect the presence of an object, the detectability metric d' was measured in each case of both small and large model lesions (Fig. 17). In all cases, images reconstructed using PICCS with statistical weighting had a noise content that interfered the least with the detection task. Interestingly, the detectability of large low-contrast objects improved for all methods as the eccentricity decreased. However, the detectability of small high contrast objects decreased slightly for PICCS with statistical weighting as the phantom became more circular.

To summarize the results from this section, the advantage of the statistical model is more apparent when the eccentricity level of the object is greater. However, when the object is approximately circular—with a semi-axis ratio above 0.85—PICCS without statistical weighting performs as well and sometimes better in terms of image quality and noise level. Finally, PICCS with statistical weighting produced

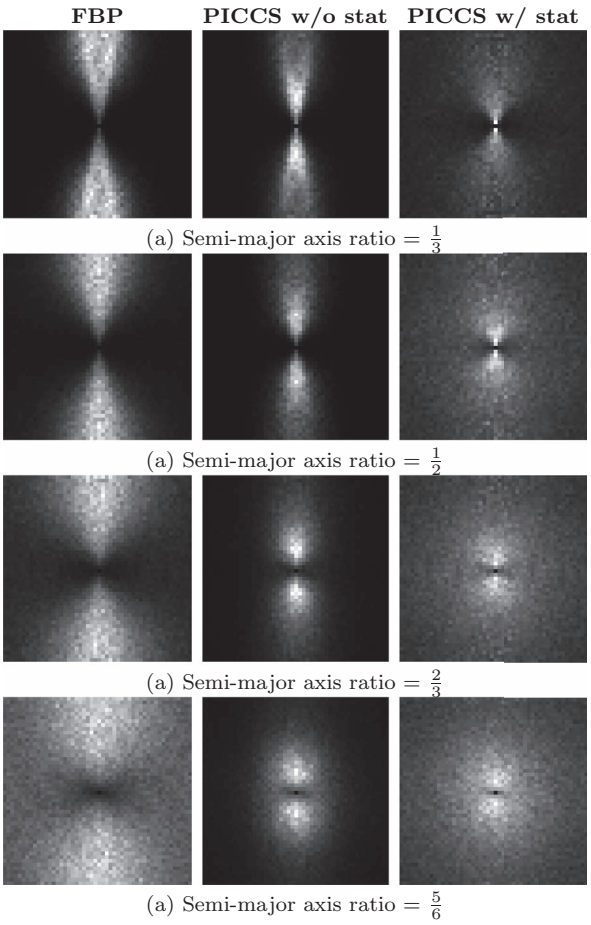

FIG. 16. Noise power spectra for numerical simulations for different levels of eccentricity. These were measured within a 50 × 50 ROI at the center of the phantom

images with the most uniform noise spatial distribution and with a NPS that interfered the least with lesion detection.

IX. CLINICAL DATASET STUDY

IX.A. Methods and materials

The *in vivo* dataset used in this study was acquired in a human subject under an institutional review board (IRB) approved protocol. The subject was a 61-year-old female who was referred for a CT cerebral perfusion scan due to an asymptomatic carotid artery stenosis. The imaging study revealed symmetric cerebral perfusion without focal perfusion deficit.

The scan was performed on a GE Discovery CT750HD scanner (GE Healthcare, Waukesha, WI) installed at the Wisconsin Institutes for Medical Research. The tube voltage was set to 80 kVp and the current to 100 mA. An exposure time of 0.4 s was used for each of 17 different time frames. Projection data from 888 detector elements acquired for each of 984 view angles separated over a full-scan angular range. Iodinated contrast agent was administered using a power injector during the scan. The reconstructed image matrix was 512 × 512 and the pixel size was $(0.625\ \text{mm})^2$.

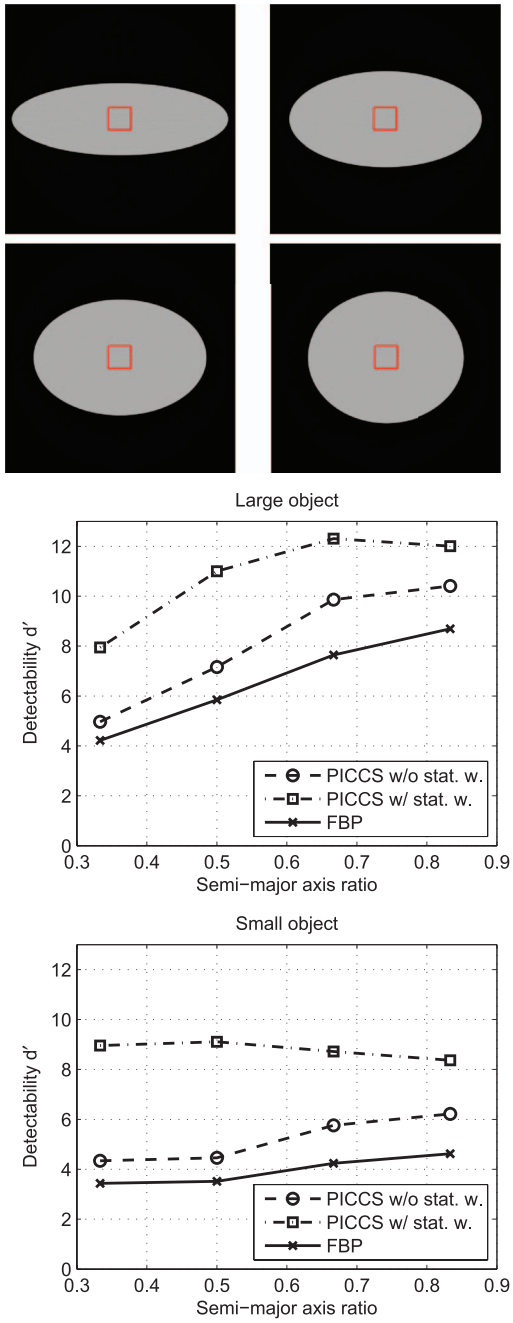

FIG. 17. Detectability for disk numerical phantom with various levels of eccentricity. The ROIs used for the measurements are shown.

IX.B. Results

We turn to the results of the human subject study. The reconstructions of this dataset are presented in Fig. 18 together with the associated maps of the standard deviation. In this case, these maps were measured among 17 different time frames. The fact that bones are visible in these maps can be explained by slight amount of misregistration between different times frames. The visibility of the vasculature was caused by the contrast dynamics. The notable feature of these maps is the value in the non-vascular tissue since in those regions, the standard deviation is dominantly caused by noise. We notice

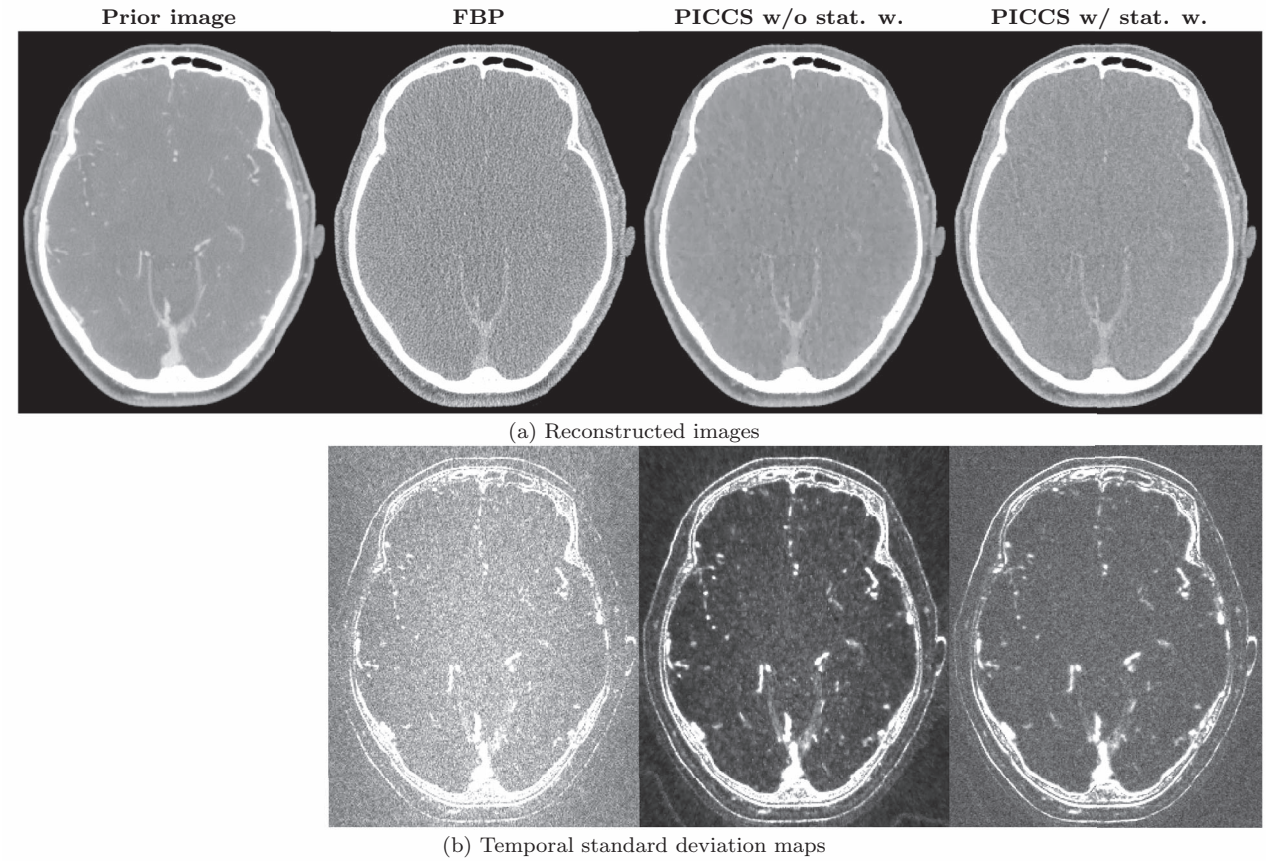

(a) Reconstructed images

(b) Temporal standard deviation maps

FIG. 18. Reconstructions for time frame 1 of *in vivo* study. The reconstructions have a display range of [−500, 500] HU while the standard deviation map have a range of [0, 100] HU.

the same trend than in numerical studies; the statistical model improved the uniformity of the noise spatial distribution.

Some quantitative metrics were measured in these datasets and the results are presented in Table II. In all cases, PICCS outperformed FBP. Furthermore, no difference was observed in terms of UQI or detectability between the two implementations of PICCS. The noise level of PICCS without the statistical weights was slightly lower than for PICCS with the statistical weight. These results are consistent with the numerical studies given that the semi-major axes ratio of the subject cranium was approximately 0.85.

Noise power spectra were measured by averaging over 17 time frames and four different ROIs each with 35 × 35 pixels and positioned in the relatively uniform corpus callosum region. The results are presented in Fig. 19. As was observed for numerical simulations, the NPS showed a higher concentration of noise in the spatial frequencies perpendicular to high noise projections. The anterior-posterior direction in this case has projections with more attenuation and thus higher noise, which explains the anisotropy of the NPS. Again, the NPS measured for reconstructions with the statistical model were less influenced by the anisotropy. There are a few caveats with respect to these NPS measurements. First, the background anatomy was not perfectly uniform; the presence of anatomical structures may have had an influence on the NPS. Furthermore, the NPS measurements assumed a 2D image volume. In reality, the geometry of the *in vivo* dataset was a single slice of a 3D volume. A more adequate methodology in that case was presented in the literature.[66] The results presented here are thus approximative, a fact that should be kept in mind when evaluating them.

TABLE II. Metrics computed for the *in vivo* datasets.

			d'	
Algorithm	UQI[a]	CNR[b]	Large object	Small object
FBP	0.134 ± 0.009	1.1	0.291	0.187
PICCS without stat. w.	0.43 ± 0.02	3.4	0.330	0.238
PICCS with stat. w.	0.44 ± 0.06	2.5	0.331	0.241

[a]Measured in uniform regions, taking the prior image as a reference.
[b]For a contrast of 80 HU.

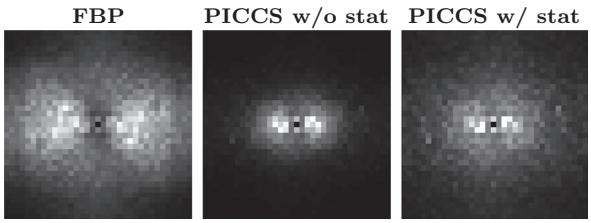

FIG. 19. Noise power spectra for *in vivo* study.

To summarize this section, the results from the human subject study are consistent with the conclusions reached using the numerical studies.

X. DISCUSSION AND CONCLUSIONS

The noise characteristics of PICCS were shown to depend on the noise level contained in the data, the object's level of eccentricity and whether or not the statistical model was applied. Most differences in the characteristics were observed in the regime of low incident x-ray fluence. No substantial difference was observed between the two implementations of PICCS in the high fluence domain. Objects with a semi-major axis ratio below 0.85 were more accurately reconstructed with lower noise using the statistical implementation. Above that range, for mostly circular objects, the PICCS implementation without the statistical model yielded more accurate images and lower noise level. At all levels of eccentricity, the noise spatial distribution was more uniform and the model-observer detectability was greater for PICCS with the statistical model. The human subject study was consistent with the results obtained using numerical simulations and further demonstrated the ability of PICCS at reconstructing the correct dynamic attenuation coefficient even with a non temporally-resolved prior image.

It may seem counterintuitive that the inclusion of the noise model resulted in reconstructions with a greater level of noise in some cases. However, one must note that the data consistency parameter λ was set to the value that produced the reconstruction with the highest UQI for all numerical studies. The higher noise observed in some of the PICCS reconstructions with statistical weighting was caused by an increase in λ necessary to obtain sharp dynamic structures. The trade off between accuracy and noise with respect to variations in λ was studied to some extent in Sec. VI.A and in Thériault-Lauzier *et al.*[14] A more thorough evaluation of this trade off for the statistical model might be enlightening in future studies.

The second paper in this series will attempt to characterize noise and spatial resolution properties of the dose reduction using PICCS framework (DR-PICCS) (Refs. 8 and 9) when implemented using a statistical model.

ACKNOWLEDGMENTS

The work is partially supported by the National Institutes of Health through Grant Nos. R01EB009699 and R01 HL090776, and a doctoral scholarship from NSERC-CRSNG to P.T.L. The authors wish to thank Mrs. Kari Pulfer and Dr. Jie Tang for their assistance with the human subject study. They also want to express their gratitude to Mr. John Garrett for his editorial input.

[a]Author to whom correspondence should be addressed. Electronic mail: gchen7@wisc.edu

[1]G. Chen, J. Tang, and S. Leng, "Prior image constrained compressed sensing (PICCS): A method to accurately reconstruct dynamic CT images from highly undersampled projection data sets," Med. Phys. **35**, 660–663 (2008).
[2]S. Leng, J. Tang, J. Zambelli, B. Nett, R. Tolakanahalli, and G. Chen, "High temporal resolution and streak-free four-dimensional cone-beam computed tomography," Phys. Med. Biol. **53**, 5653–5673 (2008).
[3]G. Chen, J. Tang, and J. Hsieh, "Temporal resolution improvement using PICCS in MDCT cardiac imaging," Med. Phys. **36**, 2130–2135 (2009).
[4]J. Tang, J. Hsieh, and G. Chen, "Temporal resolution improvement in cardiac CT using PICCS (TRI-PICCS): Performance studies," Med. Phys. **37**, 4377–4388 (2010).
[5]T. Szczykutowicz and G. Chen, "Dual energy CT using slow kVp switching acquisition and prior image constrained compressed sensing," Phys. Med. Biol. **55**, 6411–6429 (2010).
[6]B. Nett, R. Brauweiler, W. Kalender, H. Rowley, and G. Chen, "Perfusion measurements by micro-CT using prior image constrained compressed sensing (PICCS): Initial phantom results," Phys. Med. Biol. **55**, 2333–2349 (2010).
[7]J. Ramirez-Giraldo, J. Trzasko, S. Leng, C. McCollough, and A. Manduca, "Non-convex prior image constrained compressed sensing (NC-PICCS)," Proc. SPIE **7622**, 76222C–76222C-8 (2010).
[8]J. Tang, P. Thériault Lauzier, and G. Chen, "Dose reduction using prior image constrained compressed sensing (DR-PICCS)," Proc. SPIE **7961**, 79612K–79612K-8 (2011).
[9]M. Lubner, P. Pickhardt, J. Tang, and G. Chen, "Reduced image noise at low-dose multidetector ct of the abdomen with prior image constrained compressed sensing algorithm," Radiology **260**, 248–256 (2011).
[10]Z. Qi and G.-H. Chen, "Extraction of tumor motion trajectories using prior image constrained compressed sensing based four-dimensional Cone Beam CT (PICCS-4DCBCT): A validation study," Med. Phys. **38**, 5530–5538 (2011).
[11]Z. Qi and G.-H. Chen, "Performance studies of PICCS based four-dimensional cone beam computed tomography (PICCS-4DCBCT)," Phys. Med. Biol. **56**, 6709–6721 (2011).
[12]J. Ramirez-Giraldo, J. Trzasko, S. Leng, L. Yu, A. Manduca, and C. McCollough, "Nonconvex prior image constrained compressed sensing (NC-PICCS): Theory and simulations on perfusion ct," Med. Phys. **38**, 2157–2167 (2011).
[13]G. Chen, P. Thériault Lauzier, J. Tang, B. Nett, S. Leng, J. Zambelli, Z. Qi, N. Bevins, A. Raval, and H. Rowley, "Time-resolved interventional cardiac C-arm cone-beam CT: An application of the PICCS algorithm," IEEE Trans. Med. Imaging **31**, 907–923 (2012).
[14]P. T. Lauzier, J. Tang, and G.-H. Chen, "Prior image constrained compressed sensing: Implementation and performance evaluation," Med. Phys. **39**, 66–80 (2012).
[15]P. T. Lauzier, J. Tang, and G.-H. Chen, "Time-resolved cardiac interventional cone-beam CT reconstruction from fully truncated projections using the prior image constrained compressed sensing (PICCS) algorithm," Phys. Med. Biol. **57**, 2461–2476 (2012).
[16]J. Stayman, W. Zbijewski, Y. Otake, A. Uneri, S. Schafer, J. Lee, J. Prince, and J. Siewerdsen, "Penalized-likelihood reconstruction for sparse data acquisitions with unregistered prior images and compressed sensing penalties," Proc. SPIE **7961**, 79611L–79611L-6 (2011).
[17]R. Kashyap and M. Mittal, "Picture reconstruction from projections," IEEE Trans. Comput. **C-24**, 915–923 (1975).
[18]A. J. Rockmore and A. Macovski, "A maximum likelihood approach to transmission image reconstruction from projections," Nuclear Science, IEEE Trans. Nucl. Sci. **24**, 1929–1935 (1977).
[19]K. Lange and R. Carson, "EM reconstruction algorithms for emission and transmission tomography," J. Comput. Assist. Tomogr. **8**, 306–316 (1984).
[20]K. Sauer and C. Bouman, "A local update strategy for iterative reconstruction from projections," IEEE Trans. Signal Process. **41**, 534–548 (1993).
[21]S. Manglos, G. Gagne, A. Krol, F. Thomas, and R. Narayanaswamy, "Transmission maximum-likelihood reconstruction with ordered subsets for cone beam CT," Phys. Med. Biol. **40**, 1225–1241 (1995).
[22]C. Bouman and K. Sauer, "A unified approach to statistical tomography using coordinate descent optimization," IEEE Trans. Image Process. **5**, 480–492 (1996).
[23]C. Kamphuis and F. Beekman, "Accelerated iterative transmission ct reconstruction using an ordered subsets convex algorithm," IEEE Trans. Med. Imaging **17**, 1101–1105 (1998).
[24]H. Erdogan and J. Fessler, "Ordered subsets algorithms for transmission tomography," Phys. Med. Biol. **44**, 2835–2851 (1999).
[25]J. Thibault, K. Sauer, C. Bouman, and J. Hsieh, "A three-dimensional statistical approach to improved image quality for multislice helical CT," Med. Phys. **34**, 4526–4544 (2007).

[26]L. Axel, "Cerebral blood flow determination by rapid-sequence computed tomography: Theoretical analysis," Radiology **137**, 679–686 (1980).
[27]M. Koenig, E. Klotz, B. Luka, D. Venderink, J. Spittler, and L. Heuser, "Perfusion CT of the brain: Diagnostic approach for early detection of ischemic stroke," Radiology **209**, 85–93 (1998).
[28]E. Klotz and M. Konig, "Perfusion measurements of the brain: Using dynamic CT for the quantitative assessment of cerebral ischemia in acute stroke," Eur. J. Radiol. **30**, 170–184 (1999).
[29]D. Nabavi, A. Cenic, R. Craen, A. Gelb, J. Bennett, R. Kozak, and T. Lee, "CT assessment of cerebral perfusion: Experimental validation and initial clinical experience," Radiology **213**, 141–149 (1999).
[30]J. Rumberger, A. Feiring, M. Lipton, C. Higgins, S. Ell, and M. Marcus, "Use of ultrafast computed tomography to quantitate regional myocardial perfusion: A preliminary report," J. Am. Coll. Cardiol. **9**, 59–69 (1987).
[31]C. Wolfkiel, J. Ferguson, E. Chomka, W. Law, I. Labin, M. Tenzer, M. Booker, and B. Brundage, "Measurement of myocardial blood flow by ultrafast computed tomography," Circulation **76**, 1262–1273 (1987).
[32]M. Wintermark, W. Smith, N. Ko, M. Quist, P. Schnyder, and W. Dillon, "Dynamic perfusion CT: optimizing the temporal resolution and contrast volume for calculation of perfusion ct parameters in stroke patients," Am. J. Neuroradiol. **25**, 720–729 (2004).
[33]A. Kämena, F. Streitparth, C. Grieser, L. Lehmkuhl, B. Jamil, K. Wojtal, J. Ricke, and M. Pech, "Dynamic perfusion CT: optimizing the temporal resolution for the calculation of perfusion ct parameters in stroke patients," Eur. J. Radiol. **64**, 111–118 (2007).
[34]M. Supanich, Y. Tao, B. Nett, K. Pulfer, J. Hsieh, P. Turski, C. Mistretta, H. Rowley, and G. Chen, "Radiation dose reduction in time-resolved CT angiography using highly constrained back projection reconstruction," Phys. Med. Biol. **54**, 4575–4593 (2009).
[35]X. Liu, A. Primak, J. Krier, L. Yu, L. Lerman, and C. McCollough, "Renal perfusion and hemodynamics: Accurate in vivo determination at CT with a 10-fold decrease in radiation dose and hyper noise reduction1," Radiology **253**, 98–105 (2009).
[36]J. Bushberg, *The Essential Physics of Medical Imaging* (Williams and Wilkins, 2002).
[37]B. R. Whiting, "Signal statistics in x-ray computed tomography," Proc. SPIE **4682**, 53–60 (2002).
[38]J. Tang, B. Nett, and G. Chen, "Performance comparison between total variation (TV)-based compressed sensing and statistical iterative reconstruction algorithms," Phys. Med. Biol. **54**, 5781–5804 (2009).
[39]J. A. Fessler, "Statistical Reconstruction in CT," SPIE Medical Imaging Workshop (2011); see: http://web.eecs.umich.edu/~fessler/papers/files/talk/11/spie.pdf.
[40]S. Ramani and J. Fessler, "A splitting-based iterative algorithm for accelerated statistical x-ray CT reconstruction," IEEE Trans. Med. Imaging **31**, 677–688 (2012).
[41]E. Candès, J. Romberg, and T. Tao, "Robust uncertainty principles: Exact signal reconstruction from highly incomplete frequency information," IEEE Trans. Inf. Theory **52**, 489–509 (2006).
[42]E. Candès, J. Romberg, and T. Tao, "Stable signal recovery from incomplete and inaccurate measurements," Commun. Pure Appl. Math. **59**, 1207–1223 (2006).
[43]D. Donoho, "Compressed sensing," IEEE Trans. Inf. Theory **52**, 1289–1306 (2006).
[44]L. Rudin, S. Osher, and E. Fatemi, "Nonlinear total variation based noise removal algorithms," Physica D **60**, 259–268 (1992).
[45]J. Song, Q. Liu, G. Johnson, and C. Badea, "Sparseness prior based iterative image reconstruction for retrospectively gated cardiac micro-CT," Med. Phys. **34**, 4476–4483 (2007).
[46]E. Sidky and X. Pan, "Image reconstruction in circular cone-beam computed tomography by constrained, total-variation minimization," Phys. Med. Biol. **53**, 4777–4807 (2008).
[47]E. Sidky, X. Pan, I. Reiser, R. Nishikawa, R. Moore, and D. Kopans, "Enhanced imaging of microcalcifications in digital breast tomosynthesis through improved image-reconstruction algorithms," Med. Phys. **36**, 4920–4932 (2009).
[48]K. Choi, J. Wang, L. Zhu, T. Suh, S. Boyd, and L. Xing, "Compressed sensing based cone-beam computed tomography reconstruction with a first-order method," Med. Phys. **37**, 5113–5125 (2010).
[49]J. Bian, J. Siewerdsen, X. Han, E. Sidky, J. Prince, C. Pelizzari, and X. Pan, "Evaluation of sparse-view reconstruction from flat-panel-detector cone-beam CT," Phys. Med. Biol. **55**, 6575–6599 (2010).
[50]L. Ritschl, F. Bergner, C. Fleischmann, and M. Kachelrieß, "Improved total variation-based CT image reconstruction applied to clinical data," Phys. Med. Biol. **56**, 1545–1561 (2011).
[51]J. Nocedal and S. Wright, *Numerical Optimization* (Springer, 1999).
[52]R. Wagner, D. Brown, and M. Pastel, "Application of information theory to the assessment of computed tomography," Med. Phys. **6**, 83–94 (1979).
[53]L. Loo, K. Doi, and C. Metz, "A comparison of physical image quality indices and observer performance in the radiographic detection of nylon beads," Phys. Med. Biol. **29**, 837–856 (1984).
[54]K. Myers, H. Barrett, M. Borgstrom, D. Patton, and G. Seeley, "Effect of noise correlation on detectability of disk signals in medical imaging," J. Opt. Soc. Am. A **2**, 1752–1759 (1985).
[55]J. Rolland and H. Barrett, "Effect of random background inhomogeneity on observer detection performance," J. Opt. Soc. Am. A **9**, 649–658 (1992).
[56]H. Barrett, J. Yao, J. Rolland, and K. Myers, "Model observers for assessment of image quality," Proc. Natl. Acad. Sci. U.S.A. **90**, 9758–9765 (1993).
[57]A. Burgess, X. Li, and C. Abbey, "Visual signal detectability with two noise components: anomalous masking effects," Journal of the Optical Society of America A **14**(9), 2420–2442 (1997).
[58]A. Burgess, "Visual signal detection with two-component noise: Low-pass spectrum effects," Journal of the Optical Society of America A **16**(3), 694–704 (1999).
[59]F. Bochud, C. Abbey, and M. Eckstein, "Visual signal detection in structured backgrounds. iii. calculation of figures of merit for model observers in statistically nonstationary backgrounds," Journal of the Optical Society of America A **17**(2), 193–205 (2000).
[60]S. Riederer, N. Pelc, and D. Chesler, "The noise power spectrum in computed x-ray tomography," Phys. Med. Biol. **23**, 446–454 (1978).
[61]J. Baek and N. Pelc, "The noise power spectrum in CT with direct fan beam reconstruction," Med. Phys. **37**, 2074–2081 (2010).
[62]K. Hanson, "Detectability in computed tomographic images," Med. Phys. **6**, 441–451 (1979).
[63]Z. Wang and A. Bovik, "A universal image quality index," IEEE Signal Process. Lett. **9**, 81–84 (2002).
[64]J. Fessler and W. Rogers, "Spatial resolution properties of penalized-likelihood image reconstruction: Space-invariant tomographs," IEEE Trans. Image Process. **5**, 1346–1358 (1996).
[65]P. Lauzier, J. Tang, M. Speidel, and G.-H. Chen, "Noise spatial nonuniformity and the impact of statistical image reconstruction in CT myocardial perfusion imaging," Med. Phys. **39**, 4079–4092 (2012).
[66]J. Siewerdsen, I. Cunningham, and D. Jaffray, "A framework for noise-power spectrum analysis of multidimensional images," Med. Phys. **29**, 2655–2671 (2002).